IMU Self-Calibration Using Factorization

Myung Hwangbo, *Student Member, IEEE,* Jun-Sik Kim, *Member, IEEE,* and Takeo Kanade, *Fellow, IEEE*

Abstract—This paper presents a convenient self-calibration method for an IMU (Inertial Measurement Unit) using matrix factorization. Using limited information about applied loads (accelerations or angular rates) available from natural references, the proposed method can linearly solve all the parameters of an IMU in any configuration of its inertial components.

Our factorization-based calibration method exploits the bilinear form of an IMU measurement, which is the product of intrinsic calibration parameters and exerted loads. For a redundant IMU, we prove that partial knowledge of the loads, such as magnitude, can produce a linear solution space for a proper decomposition of the measurement. Theoretical analysis on this linear space reveals that a one-dimensional null space should be considered when load magnitudes are all equal (*e.g.* gravity loads). Degenerate load distributions are also geometrically identified to avoid singular measurement collection.

Since a triad IMU has a lower number of sensor components than a four-dimensional parameter space, we propose an iterative factorization in which only initial bias is required. A wide convergence region of the bias can provide an automatic setting of the initial bias as the mean of the measurements.

Performance of the proposed method is evaluated with respect to various noise levels and constraint types. Self-calibration capability is demonstrated using natural references, which are gravity for accelerometers and image stream from an attached camera for gyroscopes. Calibration results are globally optimal and identical with those of nonlinear optimization.

Index Terms—Calibration and identification, self-calibration, redundant and triad IMU, factorization method, linear algorithm

I. INTRODUCTION

An IMU (Inertial Measurement Unit) has been widely used for inertial navigation of moving vehicles and motion detection of hand-held devices. IMUs are commonly referred to as tri-axial sensor clusters since a minimal setup to sense 3D motion requires three accelerometers and three gyroscopes aligned to each orthogonal axis ($n = 3$, n is the number of sensor components). The deliberate redundancy ($n \geq 4$) like a tetrahedron[1] and other polyhedrons[2]–[5] shown in Fig. 1 has also been studied for fault-tolerance in safety-critical military and space operations as well as for innovative sensor arrangement such as an all-accelerometer unit capable of measuring angular velocity[5].

One long-standing problem of these custom designed IMUs is calibration, which is aggravated by a skewed alignment of

M. Hwangbo is a corresponding author.

M. Hwangbo and T. Kanade are with the Robotics Institute of Carnegie Mellon University, 5000 Forbes Ave, Pittsburgh, PA 15215, USA. (e-mail: myung@cs.cmu.edu; tk@cs.cmu.edu)

J.-S. Kim is with Korea Institute of Science and Technology, Seoul, Korea. (e-mail: junsik.kim@kist.re.kr)
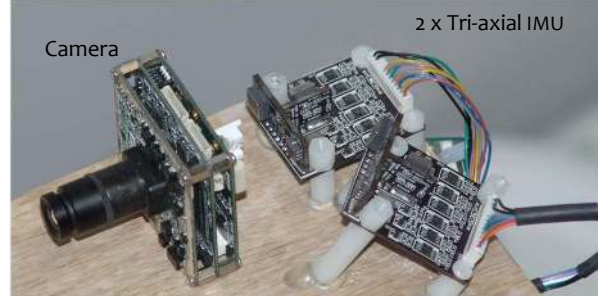
Fig. 1. An experimental system for the IMU self-calibration: A redundant IMU ($n = 6$) consists of two tri-axial MEMS-based IMUs in a skewed alignment. A camera is commonly equipped with the IMU in most sensor systems and can provide constraints for gyroscope calibration.

redundant sensor components like Fig. 1. This calibration is the parameter estimation of bias, scale factor, and alignment of every inertial sensor component in order to identify a transformation from raw measurements to acceleration or angular velocity in 3D. Traditional calibration methods[6]–[11] are precise, but require expertise, labor, time and specialized equipment. A key and often costly process in such methods involves obtaining complete knowledge of true motions (loads) exerted on the IMU.

One recent prevalent response to these challenges is self-calibration, which requires no artificial calibration object or user interaction[12]–[15]. This method exerts an abundant set of readily attainable loads on the IMU and finds calibration parameters that match with partially known information about the exerted motions. For instance, gravity is always exerted on accelerometers and its magnitude is known. Once measurements are collected at various attitudes with respect to gravity in a static condition, the gravity magnitude provides a sufficient constraint for a parameter search. Common drawbacks of this approach are that it is based on nonlinear optimization, not scalable for a large number of sensor components, and limited to a specific sensor configuration. Hence, the issues we will address in self-calibration are: (1) finding a linear solution that requires no initial parameters, (2) extending to any triad or redundant configurations, (3) providing a generalized description on partially known motion.

A new perspective on the self-calibration problem has been explored through the factorization method[16]–[18], originally invented for 3D reconstruction of camera motions and scene objects from multi-view images in computer vision[19]. The factorization-based calibration proposed in this paper takes advantage of a bilinear form of IMU measurement. In other words, IMU measurement can be decomposed as the product of intrinsic calibration parameters (bias, scale factor and alignment) and exerted loads (accelerations or angular velocities). Hence, IMU calibration becomes equivalent to recovering these original factors producing given measurements, based on

partial information about applied loads, such as magnitudes. Note that finding a linear solution for this recovery is not trivial but challenging because the IMU measurement model is *affine* due to the bias.

In the factorization method, the parameter dimension per component cannot exceed the number of sensor components. Since the IMU's parameter dimension is four, we will prove that a linear solution exists for a redundant IMU ($n \geq 4$) which has extra components. One interesting property we will present regarding the linear solution space is that a one-dimensional null space exists when solely the gravity magnitude is used for accelerometer calibration. Thus, more intriguing properties, such as degenerate load set, will be investigated through theoretical analysis of this solution space.

For a triad IMU ($n = 3$), we will propose an iterative factorization method in which its bias is excluded for dimension reduction and then separately updated based on the factorization error resulting from incorrect bias compensation. Compared to other nonlinear methods [12]–[15], this iterative method requires only an initial bias, and its convergence region is wide enough to automatically set an initial bias as the mean of the measurements.

The main contributions and features of the factorization-based IMU calibration approach presented in this paper are summarized as follows:

- Accelerometer self-calibration using gravity
- Gyroscope self-calibration using image feature tracks
- Linear solution for a redundant IMU
- Iterative linear solution for a triad IMU (initial bias only)
- Identification of degenerate calibration load sets

In Fig. 1, a camera affixed to the IMU is used to provide constraints for gyroscope self-calibration. We will obtain the magnitude of angular velocity from images containing distant scene objects [20].

II. RELATED WORK

Traditionally, IMU calibration requires complete load identification. A robotic manipulator [6] or special mechanical platform [7] were used for precise realization of the desired orientation of an IMU. Diesel [8] proposed a rotation sequence of nine orientation points for tri-axial IMUs, and Nebot and Durrant-Whyte [9] initialized bias and alignment using GPS data. IMU mechanization states (position, velocity and orientation) are compared with external high-precision devices, such as optical position tracking systems [10] [11] or speed-controlled turning tables [3]. In fusion of an IMU and other absolute sensors like GPS, calibration has been casted as a state estimation problem using the Kalman filter [21]–[25].

In accelerometer self-calibration using gravity, Skog and Händel [13] and Syed *et al.* [14] presented nonlinear least-squares solutions which minimize magnitude errors. Since convergence region was small in their work, a procedure to flip over an IMU was required in order to find an initial parameter [14]. Won and Golnaraghi [15] enlarged the convergence region using a sophisticated iterative method. Drawbacks of

these nonlinear methods are primarily related to the fact that all calibration parameters are searched at the same time, requiring a small initial error. Furthermore, their sensor configuration models are not universal, but specific to a tri-axial IMU, thus not scalable for additional sensor components.

The factorization method was first introduced by Tomasi and Kanade [19] [26] for 3D reconstruction of camera motions and scene objects based on feature tracking of an orthographic camera. Since factorization exploits a bilinear formulation of image measurements, it has inspired new approaches in other domains where a similar bilinear formulation is available, for example, force/torque sensor calibration [16], [17], [27] and object color modeling [28]. The most relevant work to our proposed method is the shape-from-motion [16] [17] presented by Voyles *et al.* This calibration scheme applies a few load weights on a force/torque sensor at various directions, and decomposes a large volume of raw measurements into a load matrix and shape matrix of all the strain-gauge components using known load magnitudes. Our initial work on IMU calibration [18] focused on applying factorization to a redundant configuration using motion magnitudes and orthogonal motions generated by a right-angle iron. In this paper, we present a comprehensive approach for self-calibration for both redundant and triad IMUs through additional rigorous analysis on a linear solution space.

From a mathematical point of view, our essential achievement in the factorization method is the identification of a linear solution space even in cases when a measurement model is affine due to a non-zero bias. While a reconstruction matrix ($\mathbf{Q}$ in Section V) was found by a nonlinear cylindrical fitting in the shape-from-motion [17], our rank analysis on a solution space reveals that $\mathbf{Q}$ is not only linearly solvable but also has a special case where an one-dimensional null space is present if all the load constraints have the same magnitude.

III. PROBLEM FORMULATION

This section provides an overview of our factorization method based on the bilinear formulation of IMU measurements. Since no differences exist between the use of accelerometers or gyroscopes as an inertial sensor, motion refers to either force (acceleration) $\mathbf{f}$ or angular velocity $\boldsymbol{\omega}$ exerted on the IMU. In addition, the terms, *motion* and *load*, are identical and will be used interchangeably.

A. Affine measurement model

Suppose that the IMU is an accelerometer (or gyroscope) cluster of n single-axis components and its components are arbitrarily aligned to each other, as shown in Fig. 2.

A measurement model of each component z is *affine*, $z = af + b$, *i.e.*, linearly proportional to an external motion f and a non-zero b for null motion. In 3D, the measurement z_i of an i-th component in the IMU is expressed as the sum of the projection of a motion $\mathbf{f}$ on the sensitivity axis $\mathbf{s}_i$ and the non-zero bias b_i in an IMU local coordinate:

$$z_i = \mathbf{f}^\top \mathbf{s}_i + b_i, \quad i = 1, \ldots, n \tag{1}$$

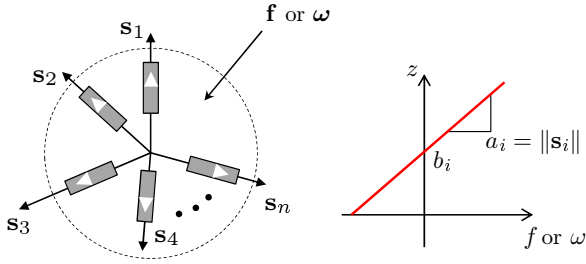where the scale factor $a_i = \|\mathbf{s}_i\|$.

Fig. 2. (Left) An accelerometer or gyroscope unit composed of n single-axis components in an arbitrary configuration. (Right) An affine measurement model ($z = a_i f + b_i$) of a single-axis inertial sensor component with the scale factor $a_i = \|\mathbf{s}_i\|$ and the bias b_i.

B. Bilinear Form

Once m motions are applied on the n-component IMU, the measurements are collected into a matrix $\mathbf{Z} \in \mathcal{R}^{m \times n}$ as follows:

$$\mathbf{Z} = \begin{bmatrix} \mathbf{f}_1^\top \mathbf{s}_1 + b_1 & \mathbf{f}_1^\top \mathbf{s}_2 + b_2 & \cdots & \mathbf{f}_1^\top \mathbf{s}_n + b_n \\ \mathbf{f}_2^\top \mathbf{s}_1 + b_1 & \mathbf{f}_2^\top \mathbf{s}_2 + b_2 & \cdots & \mathbf{f}_2^\top \mathbf{s}_n + b_n \\ \vdots & \vdots & & \vdots \\ \mathbf{f}_m^\top \mathbf{s}_1 + b_1 & \mathbf{f}_m^\top \mathbf{s}_2 + b_2 & \cdots & \mathbf{f}_m^\top \mathbf{s}_n + b_n \end{bmatrix} \quad (2)$$

where z_{ij} is the j-th component's output for the i-th motion $\mathbf{f}_i$ ($i = 1, \ldots, m$, $j = 1, \ldots, n$).

The measurement matrix $\mathbf{Z}$ can be rewritten as a product of two matrices, $\mathbf{F}_b$ and $\mathbf{S}_b$[1], which are called an *augmented motion* matrix and a *shape* matrix [19], respectively. Each measurement z_{ij} is a product of an augmented motion vector $[\mathbf{f}_i^\top \ 1]$ and a shape parameter $[\mathbf{s}_j^\top \ b_j]$.

$$\mathbf{Z} = \begin{bmatrix} \mathbf{f}_1^\top & 1 \\ \mathbf{f}_2^\top & 1 \\ \vdots & \vdots \\ \mathbf{f}_m^\top & 1 \end{bmatrix} \begin{bmatrix} \mathbf{s}_1 & \mathbf{s}_2 & \cdots & \mathbf{s}_n \\ b_1 & b_2 & \cdots & b_n \end{bmatrix} = \begin{bmatrix} \mathbf{F} & \mathbf{1} \end{bmatrix} \begin{bmatrix} \mathbf{S} \\ \mathbf{b} \end{bmatrix} = \mathbf{F}_b \mathbf{S}_b \quad (3)$$

If the external calibration device used in a traditional calibration method precisely captures all the motions ($\mathbf{f}_1, \ldots, \mathbf{f}_m$), the calibration parameter could become as simple as a least squares solution, $\mathbf{S}_b = \mathbf{F}_b^+ \mathbf{Z} = (\mathbf{F}_b^\top \mathbf{F}_b)^{-1} \mathbf{F}_b^\top \mathbf{Z}$ when $m \geq 4$.

Contrarily, in the factorization method, calibration aims at estimating $\mathbf{S}_b$ from partially known motions, which are readily obtainable without the use of calibration devices.

C. Reconstruction constraints

Given $\mathbf{Z}$, constraints are required for finding the true motion and shape matrix since there exist infinitely many factorizations that can decompose $\mathbf{Z}$ into a product of two matrices.

The first constraint is a matrix rank condition on $\mathbf{Z}$. Let p denote the dimension of calibration parameters per component in $\mathbf{S}_b$ ($p = 4$). Since $\mathbf{Z}$ is constructed from $\mathbf{F}_b \in \mathcal{R}^{m \times p}$ and $\mathbf{S}_b \in \mathcal{R}^{p \times n}$, the rank of $\mathbf{Z}$ should be at most p when $\min(m, n) \geq p$ and when $\mathbf{Z}$ is noiseless. This is called the *proper rank constraint* [19]. Singular value decomposition

---

[1] The subscript b is intended to clarify that the bias b is explicitly considered in the shape matrix while the motion matrix is augmented with an extra column of ones on the right.

(SVD) [29] can be used to factor $\mathbf{Z}$ into two rank-p matrices, $\widehat{\mathbf{F}_b}$ and $\widehat{\mathbf{S}_b}$, as follows:

$$\mathbf{Z} = \mathbf{U} \Sigma \mathbf{V}^\top = (\mathbf{U} \Sigma^{1/2})(\Sigma^{1/2} \mathbf{V}^\top) = \widehat{\mathbf{F}_b} \widehat{\mathbf{S}_b} \quad (4)$$

where Σ is a $p \times p$ diagonal, $\mathbf{U}$ and $\mathbf{V}$ are an $m \times p$ and $n \times p$ unitary matrix, respectively. An ambiguity remains because it is possible to insert any invertible matrix $\mathbf{A}_{4 \times 4}$ inbetween:

$$\mathbf{Z} = \widehat{\mathbf{F}_b} \widehat{\mathbf{S}_b} = (\widehat{\mathbf{F}_b} \, \mathbf{A}_{4 \times 4})(\mathbf{A}_{4 \times 4}^{-1} \, \widehat{\mathbf{S}_b}) = \mathbf{F}_b \mathbf{S}_b \quad (5)$$

The second constraint is drawn from partially known calibrating motions ($\mathbf{f}_1, \ldots, \mathbf{f}_m$). Suppose that each piece of information about motions is expressed as an inner product:

$$\mathbf{f}_i^\top \mathbf{f}_j = c_{ij} \quad (6)$$

which represents a partial knowledge of a pair of motions or a single motion such as motion magnitude $\|\mathbf{f}_i\|^2 = c_{ii}$ or orthogonal motion $\mathbf{f}_i^\top \mathbf{f}_j = 0$ [18]. We call a set of such motion constraints a *load constraint set* $\mathcal{C}$. A procedure for finding $\mathbf{A}_{4 \times 4}$ from constraint set $\mathcal{C}$ is a key step in factorization and will be explained in detail in Section V.

Finally, once $\mathbf{A}_{4 \times 4}$ is obtained from $\mathcal{C}$, the calibration step is completed from the simultaneous recovery of the shape parameters in $\mathbf{S}_b$ and applied motions in $\mathbf{F}_b$ as follows.

$$\mathbf{S}_b = \mathbf{A}_{4 \times 4}^{-1} \widehat{\mathbf{S}_b}, \quad \mathbf{F}_b = \widehat{\mathbf{F}_b} \mathbf{A}_{4 \times 4} \quad (7)$$

D. Redundant IMU vs. triad IMU

The proper rank constraint demands that the number of components (n) should be no less than the shape parameter dimension ($p = 4$), *i.e.*, $n \geq p$. This constraint is satisfied by a redundant IMU ($n \geq 4$) but violated by a triad IMU ($n = 3$). In other words, the SVD in (4) fails to produce an $\widehat{\mathbf{S}_b} \in \mathcal{R}^{p \times n}$ when $p = 4$ and $n = 3$.

One possible workaround for a triad IMU is reducing the parameter dimension to $p = 3$ by excluding the bias $\mathbf{b}$ from $\mathbf{S}_b$ and iteratively estimating the bias from the factorization error. An iterative factorization method for a triad IMU will be presented in Section VII.

IV. NATURAL REFERENCES

One significant merit of our factorization method is that knowledge of load magnitudes is sufficient to calibrate an IMU with no initial parameters. This enables a self-calibration procedure using load magnitudes that are readily obtainable in nature. We introduce the gravity and distant scene objects viewed in a camera as natural references and will validate them in experiments.

A. Intra-relation load constraint set $\mathcal{C}^*$

We first define the intra-relation constraint set $\mathcal{C}^*$ since the case $i = j$ in (6) is considered for load magnitudes. For inter-relation load constraints, see Appendix B or [18] for an orthogonal case $c_{ij} = 0$.

Definition 1. $\mathcal{C}^*$ *is an intra-relation load constraint set which is composed only of load magnitudes,* i.e., $\mathcal{C}^* = \{c_{ii} = \mathbf{f}_i^\top \mathbf{f}_i \,|\, i = 1, \ldots, m\}$. *Also,* $\mathcal{C}_\tau^*$ *refers to a constraint set when all the magnitudes in* $\mathcal{C}^*$ *are equal,* i.e., $c_{ii} = \tau$ *for all* i.
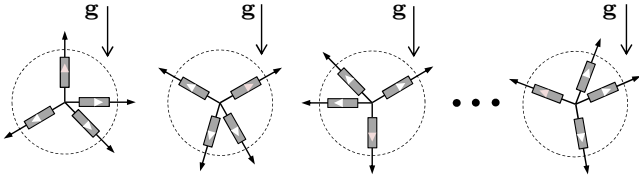
Fig. 3. Gravity magnitude constraint $\mathcal{C}^*_{\tau=1}$ for the accelerometer self-calibration: an accelerometer unit is oriented at different attitudes with respect to gravity in a static condition. ($\|\mathbf{f}_i\| = g$, for all i)
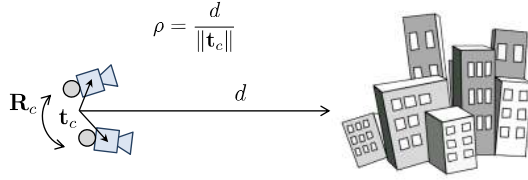

Fig. 4. Angular speed constraint $\mathcal{C}^*$ for the gyroscope self-calibration: a camera affixed to a gyroscope unit is randomly rotated in front of distant scene objects. The angular speed $\|\boldsymbol{\omega}\|$ is obtained from feature correspondences between two consecutive images and a known time interval.

B. Gravity magnitude for accelerometer calibration

Suppose that an IMU is arbitrarily placed at m different orientations in a static condition as shown in Fig. 3. Although the direction of each load $\mathbf{f}_i$ is unknown, its magnitude is known as $\|\mathbf{f}_i\| = g$ for $i = 1, \ldots, m$ since an accelerometer unit is exposed to the identical force (gravity $\mathbf{g}$).

This gravity magnitude constraint can be denoted by $\mathcal{C}^*_{\tau=1}$ from Definition 1 (a known constant magnitude is scaled to 1 without loss of generality). Interesting properties of a solution space for $\mathcal{C}^*_{\tau=1}$ will be discussed in Section VI.

C. Camera rotation speed for gyroscope calibration

To obtain the magnitude of an angular velocity $\boldsymbol{\omega}$ exerted on an IMU, we use a camera affixed to the IMU like Fig. 1. The camera's rotation speed $\|\boldsymbol{\omega}_c\|$ is, which is the same as $\|\boldsymbol{\omega}\|$ regardless of coordinate system, can be obtained when feature correspondence $(\mathbf{x}_1, \mathbf{x}_2)$ between two images (I_1, I_2) and its time interval Δt are given.

For a camera motion that purely rotates by $\mathbf{R}_c$ (no translation, $\mathbf{t}_c = \mathbf{0}$), there exists an infinite homography $\mathbf{H}$:

$$\mathbf{x}_1 \cong \mathbf{H}\mathbf{x}_2, \quad \mathbf{H} = \mathbf{K}\mathbf{R}_c\mathbf{K}^{-1} \tag{8}$$

where $\cong$ is an up-to-scale equality in homogeneous coordinates and $\mathbf{K}$ is a camera calibration matrix [20].

Suppose $\mathbf{H}$ is estimated from a given set of feature correspondences $\{\mathbf{x}_1^i, \mathbf{x}_2^i\}$. Since $\mathbf{H}$ and $\mathbf{R}_c$ are *similar* matrices for $\mathbf{K}$ in (8) and they share the same eigenvalues [29], we have $\mathrm{eig}(\mathbf{H}) = (1, e^{j\theta_c}, e^{-j\theta_c})$ where θ_c is the rotation angle of $\mathbf{R}_c$ and $\|\boldsymbol{\omega}\| = \theta_c/\Delta t$. When the IMU is randomly rotated m times, a load constraint $\mathcal{C}^* = (\|\boldsymbol{\omega}_1\|, \ldots, \|\boldsymbol{\omega}_m\|)$ is prepared for the factorization method.

When scene objects are distant, it is possible to relax the rotating camera in (8) to $\mathbf{t}_c \neq \mathbf{0}$. An error in θ_c is negligible if $\rho = d/\|\mathbf{t}_c\| \geq 500$ in Fig. 4 (see Section VIII for more details). Note that there is no need for calibrating the camera or placing a known calibration object.

V. Redundant IMU Calibration

The calibration problem is now equivalent to finding a non-singular matrix $\mathbf{A}_{4\times4}$ in (5). Given a load constraint set $\mathcal{C}$, a linear solution for $\mathbf{A}_{4\times4}$ will be presented when an IMU has a redundant sensor configuration ($n \geq 4$).

A. Shape recovery using load constraints

Given the load constraint set $\mathcal{C}$ in (6), a set of linear constraints for $\mathbf{A}_{4\times4}$ in (5) are constructed. Let $\mathbf{A}_{4\times4}$ be partitioned into the following block matrices.

$$\mathbf{A}_{4\times4} = \begin{bmatrix} \mathbf{A}_{4\times3} & \mathbf{a}_4 \end{bmatrix} = \begin{bmatrix} \mathbf{A}_{3\times3} & \mathbf{a}_4 \\ \mathbf{u}^\top & \end{bmatrix} \tag{9}$$

Firstly, the last column $\mathbf{a}_4$ is immediately recoverable without use of $\mathcal{C}$. Since the last column of $\mathbf{F}_b = [\mathbf{F}\ \mathbf{1}]$ is constant, the pseudo-inverse of $\widehat{\mathbf{F}}_b$ finds a least squares solution for $\mathbf{a}_4$:

$$\mathbf{a}_4 = \widehat{\mathbf{F}}_b^+ \mathbf{1} \tag{10}$$

Secondly, the remaining columns $\mathbf{A}_{4\times3}$ are associated with $\mathcal{C}$. From (7), each true load $\mathbf{f}_i \in \mathcal{R}^{3\times1}$ is rewritten as

$$\mathbf{f}_i = \mathbf{A}_{4\times3}^\top \widehat{\mathbf{f}}_{b,i} \quad \text{for } i = 1, \ldots, m \tag{11}$$

where $\widehat{\mathbf{f}}_{b,i} \in \mathcal{R}^{4\times1}$ is at the i-th row of $\widehat{\mathbf{F}}_b$.

Suppose that k load constraints exist in $\mathcal{C}$. Plugging (11) into each load constraint c_{ij} yields a quadratic equation for $\mathbf{A}_{4\times3}$. The Kronecker product $\otimes$ rewrites this as a linear equation in terms of $\mathbf{q} \in \mathcal{R}^{10\times1}$, which is a vector of lower triangular elements in a symmetric matrix $\mathbf{Q} = \mathbf{A}_{4\times3}\mathbf{A}_{4\times3}^\top$:

$$c_{ij} = \mathbf{f}_i^\top \mathbf{f}_j = \widehat{\mathbf{f}}_{b,i}^\top (\mathbf{A}_{4\times3}\mathbf{A}_{4\times3}^\top) \widehat{\mathbf{f}}_{b,j} = \widehat{\mathbf{f}}_{b,i}^\top \mathbf{Q}\, \widehat{\mathbf{f}}_{b,j} \tag{12}$$

$$= [\widehat{\mathbf{f}}_{b,i} \otimes \widehat{\mathbf{f}}_{b,j}]^\top \mathrm{vec}(\mathbf{Q}) = [\widehat{\mathbf{f}}_{b,i} \otimes \widehat{\mathbf{f}}_{b,j}]^\top \mathbf{T}_{16\times10}\,\mathbf{q} \tag{13}$$

where $\mathbf{T}_{16\times10}$ is a constant matrix that converts a vectorized $\mathbf{Q}$ into a minimal parameter $\mathbf{q}$ (see Appendix A for details on $\mathbf{q}$ and $\mathbf{T}_{16\times10}$). Stacking all the constraints in $\mathcal{C}$ produces a linear system equation $\mathbf{L} \in \mathcal{R}^{k\times10}$ for $\mathbf{q}$:

$$\mathbf{c} = \mathbf{L}\,\mathbf{q} \tag{14}$$

where $\mathbf{L} = \mathcal{S}[\widehat{\mathbf{f}}_{b,i} \otimes \widehat{\mathbf{f}}_{b,j}]^\top \mathbf{T}_{16\times10}$, $\mathbf{c}$ is a vector of $\{c_{ij}\}$ in $\mathcal{C}$, and $\mathcal{S}$ is a row stacking operator that uses all the constraints in $\mathcal{C}$.

It is noteworthy that $\mathbf{Q} \in \mathcal{R}^{4\times4}$ is not a full-rank but rank-3 matrix because $\mathrm{rank}(\mathbf{Q}) = \mathrm{rank}(\mathbf{A}_{4\times3}) = 3$. Rewriting $\mathbf{Q}$ using the block matrices in (9)

$$\mathbf{Q} = \begin{bmatrix} \mathbf{A}_{3\times3}^\top \mathbf{A}_{3\times3} & \mathbf{A}_{3\times3}^\top \mathbf{u} \\ \mathbf{u}^\top \mathbf{A}_{3\times3} & \mathbf{u}^\top \mathbf{u} \end{bmatrix} \triangleq \begin{bmatrix} \mathbf{Q}_{3\times3} & \mathbf{q}_{13} \\ \mathbf{q}_{13}^\top & q_{44} \end{bmatrix} \tag{15}$$

reveals that $\mathbf{Q}$ (equivalently $\mathbf{q}$) is internally subject to the following two constraints, which we call a *q-constraint*:

$$\det(\mathbf{Q}) = 0 \tag{16a}$$

$$\min\{\mathrm{eig}(\mathbf{Q}_{3\times3})\} > 0 \tag{16b}$$

where the first rank constraint[2] is due to a non-invertible rank-3 $\mathbf{Q}$, and the second positivity constraint indicates that $\mathbf{Q}_{3\times3} =$

---

[2]This nonlinear constraint can be rewritten as $\mathbf{q}_{13}^\top \mathbf{Q}_{3\times3}^{-1} \mathbf{q}_{13} - q_{44} = 0$.
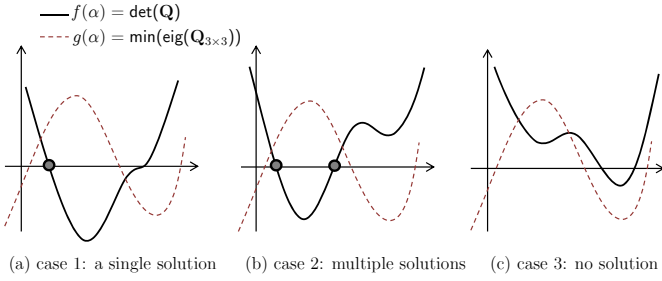
(a) case 1: a single solution   (b) case 2: multiple solutions   (c) case 3: no solution

Fig. 5. Three cases of the number of solutions for $\mathbf{q}$ when $\mathrm{rank}(\mathbf{L}) = 9$: Among four roots of $f(\alpha)$, a true α should be real and make $\mathbf{Q}_{3\times3}$ a positive definite. A single solution exists when no noise in $\mathbf{Z}$(case 1). Multiple or no solutions for $\mathbf{q}$ may exist when there is a noise in $\mathbf{Z}$ (case 2 and 3).

$\mathbf{A}_{3\times3}^\top \mathbf{A}_{3\times3}$ is a positive definite by construction and thus its eigenvalues should be all positive.

When $\mathbf{L}$ in (14) is full-rank with a sufficient number (k) of load constraints, *i.e.*, $\mathrm{rank}(\mathbf{L}) = 10$ when $k \geq 10$, a least squares solution $\mathbf{q}$ is obtained from the pseudo-inverse of $\mathbf{L}$. In addition, when no noise is present in $\mathbf{Z}$, the following particular solution $\mathbf{q}_p$ also inherently satisfies the q-constraint.

$$\mathbf{q} = \mathbf{q}_p \quad \text{s.t.} \quad \mathbf{q}_p = \mathbf{L}^+ \mathbf{c} \qquad (17)$$

On the other hand, even when $\mathbf{L}$ is *not* full-rank, $\mathbf{q}$ is still solvable if $\mathrm{rank}(\mathbf{L}) = 9$. This is because $\mathbf{q} \in \mathcal{R}^{10\times1}$ actually has 9 degrees of freedom when the rank condition of the q-constraint (16a) is considered. The solution for $\mathbf{q}$ spans an one-dimensional null space $\mathcal{N}$ of $\mathbf{L}$ with an unknown scalar α:

$$\mathbf{q} = \mathbf{q}_p + \alpha\mathbf{q}_n \quad \text{s.t.} \quad \mathbf{q}_p = \mathbf{L}^+ \mathbf{c}, \, \mathbf{q}_n \in \mathcal{N}(\mathbf{L}). \qquad (18)$$

The rank and positivity condition in the q-constraint (16) are used to determine α. Plugging (18) into the rank condition (16a) yields a fourth-order polynomial $f(\alpha)$ whose coefficients[3] are parameterized by $\mathbf{q}_p$ and $\mathbf{q}_n$. Among up to four possible roots, a true α should be real-valued and which makes $\mathbf{Q}_{3\times3}$ a positive definite matrix as in (16b). Fig. 5 shows that three possible cases exist for the number of $\mathbf{q}$ solutions depending on the location of α. Only one α meets the q-constraint when no noise in $\mathbf{Z}$ (This will be proved later in Proposition 2 in Section VI).

Once $\mathbf{q}$ is obtained, $\mathbf{A}_{4\times3} = [\mathbf{A}_{3\times3}^\top \ \mathbf{u}]^\top$ in (9) is found via Cholesky decomposition of a symmetric positive-definite $\mathbf{Q}_{3\times3}$:

$$\mathbf{A}_{3\times3} = \mathtt{chol}(\mathbf{Q}_{3\times3}), \quad \mathbf{u} = \mathbf{A}_{3\times3}^{-\top}\mathbf{q}_{13} \qquad (19)$$

Finally, the reconstruction of true $\mathbf{S}_b$ and $\mathbf{F}_b$ is completed as (7) by the found $\mathbf{A}_{4\times4}$. Note that this final reconstruction is fundamentally ambiguous up to a three-dimensional rotation $\mathbf{R}$ since $\mathbf{Z} = \mathbf{F}\mathbf{S} + \mathbf{b} = (\mathbf{F}\mathbf{R})(\mathbf{R}^\top\mathbf{S}) + \mathbf{b}$ because a sensor's internal orthonormal coordinate system can be chosen freely. This fact is already reflected in the solution when the Cholesky decomposition of $\mathbf{Q}_{3\times3}$ in (19) determines $\mathbf{A}_{3\times3}$ up to a rotation matrix $\mathbf{R}$. See Appendix C for how to determine $\mathbf{R}$ for an external frame.

---

[3]A symbolic computation of $\det(\mathbf{Q}(\mathbf{q}_p + \alpha\mathbf{q}_n)) = 0$ produces the coefficients of a fourth-order polynomial $f(\alpha)$.

Algorithm 1: Redundant IMU calibration ($n \geq 4$)

Input: $\mathbf{Z}$, $\mathcal{C}$,   Output: $\mathbf{S}_b$

$p = 4$, $k = |\mathcal{C}|$
$[\mathbf{U}, \mathbf{S}, \mathbf{V}] = \mathtt{svd}(\mathbf{Z})$
$\widehat{\mathbf{F}_b} = \mathbf{U}_p\mathbf{\Sigma}_p^{1/2}$, $\widehat{\mathbf{S}_b} = \mathbf{\Sigma}_p^{1/2}\mathbf{V}_p^\top$
foreach c_{ij} *in* $\mathcal{C}$ **do**
    $\mathbf{L}_k = [\widehat{\mathbf{f}}_{b,i} \otimes \widehat{\mathbf{f}}_{b,j}]^\top \mathbf{T}_{16\times10}$
if $\mathcal{C} = \mathcal{C}_{\tau=1}^*$ *or* $|\mathcal{C}| = 9$ **then**
    $[\mathbf{U}, \mathbf{S}, \mathbf{V}] = \mathtt{svd}(\mathbf{L})$
    $\mathbf{q}_p = \mathbf{L}^+\mathbf{c}$, $\mathbf{q}_n = \mathtt{last\_col}(\mathbf{V})$
    $\alpha = \mathtt{q\_constraint}(\mathbf{q}_p, \mathbf{q}_n)$
    $\mathbf{Q} = \mathtt{convert}(\mathbf{q}_p + \alpha\mathbf{q}_n)$
else
    $\mathbf{q} = \mathbf{L}^+\mathbf{c}$, $\mathbf{Q} = \mathtt{convert}(\mathbf{q})$
    $[\mathbf{U}, \mathbf{S}, \mathbf{V}] = \mathtt{svd}(\mathbf{Q})$
    $\mathbf{Q} = \mathbf{U}_3\mathbf{S}_3\mathbf{V}_3$

$\mathbf{A}_{3\times3} = \mathtt{chol}(\mathbf{Q}_{3\times3})$

$\mathbf{A}_{4\times4} = \begin{bmatrix} \mathbf{A}_{3\times3} & \widehat{\mathbf{F}_b}^+ \, \mathbf{1} \\ \mathbf{q}_{13}^\top\mathbf{A}_{3\times3}^{-1} & \end{bmatrix}$

$\mathbf{S}_b = \mathbf{A}_{4\times4}^{-1}\widehat{\mathbf{S}_b}$, $\mathbf{F}_b = \widehat{\mathbf{F}_b}\,\mathbf{A}_{4\times4}$

B. Solution space

Table I summarizes the solution schemes according to $\mathrm{rank}(\mathbf{L})$ and typical examples for each scheme. One key example is that $\mathbf{L}$ is always rank deficient when the gravity magnitude is solely used in accelerometer calibration, *i.e.*, $\mathrm{rank}(\mathbf{L}) \leq 9$ when $\mathcal{C} = \mathcal{C}_{\tau=1}^*$. For gravity magnitude, Proposition 1 and 2 in Section VI-B claim that $f(\alpha)$ has one real root for a true α and triple roots which violate the positivity condition of the q-constraint (16b).

More analysis on the solution space $\mathbf{L}$ will be described in Section VI, including a minimum number of constraints $|\mathcal{C}|_{min}$ and degenerate load condition $\mathcal{D}_\mathbf{F}$.

C. Practical Issues

Since the measurement $\mathbf{Z}$ is inevitably corrupted by noise, additional steps are required to meet the assumptions made for factorization. Some considerations and caveats are:

- In the SVD of $\mathbf{Z}$ in (4), a noisy $\mathbf{Z} \in \mathcal{R}^{m\times n}$ may have a rank greater than p. The rank-p enforcement on $\mathbf{Z}$ is

$$\widehat{\mathbf{Z}} = (\mathbf{U}_p\mathbf{\Sigma}_p^{1/2})(\mathbf{\Sigma}_p^{1/2}\mathbf{V}_p^\top) = \widehat{\mathbf{F}_b}\,\widehat{\mathbf{S}_b} \qquad (20)$$

  where $\mathbf{\Sigma}_p$ is the top left $p \times p$ block of $\mathbf{\Sigma}$, and $\mathbf{U}_p$ and $\mathbf{V}_p$ are the first p columns of $\mathbf{U}$ and $\mathbf{V}$, respectively. $\widehat{\mathbf{Z}}$ is a closest rank-p matrix to $\mathbf{Z}$ in terms of the Frobenius norm.

- When $\mathrm{rank}(\mathbf{L}) = 10$, a least squares solution $\mathbf{q}_p$ (17) may result in a full-rank $\mathbf{Q}$ which violates the rank condition of the q-constraint (16a). To enforce the rank-3 $\mathbf{Q}$, the smallest singular value of $\mathbf{Q}$ is set to zero with the SVD of $\mathbf{Q}$.

- When $\mathrm{rank}(\mathbf{L}) = 9$, multiple solutions for $\mathbf{q}$ may exist (case 2 in Fig. 5) but the corresponding $\mathbf{S}_b$ values are

discriminative enough to identify inappropriate solutions which have severely distorted and warped shapes. Since the bias is generally uniform, a true solution can be selected as the one with the smallest variance of $\mathbf{b}$.

- If the measurement noise in $\mathbf{Z}$ is too high, the solution for $\mathbf{q}$ does not always produce a positive-definite $\mathbf{Q}_{3\times3}$. Thus, the Cholesky decomposition fails to obtain $\mathbf{A}_{3\times3}$. This sensitivity to noise can be reduced if further loads are made so that more constraints are used.

Algorithm 1 shows the factorization-based redundant calibration that takes these practical issues into account.

VI. ADVANCED DISCUSSION ON LINEAR SOLUTION SPACE

In this section, we discuss the linear solution space of $\mathbf{L}$ in (14) constructed by a load constraint $\mathcal{C}$ in the redundant IMU calibration.

A. Minimum number of constraints

Let $|\mathcal{C}|$ denote the number of independent constraints found in $\mathcal{C}$. The factorization is equivalent to finding the $\mathbf{q}$ subject to the q-constraint (16). The degrees of freedom of $\mathbf{q} \in \mathcal{R}^{10\times1}$ is nine because $\mathbf{A}_{3\times3}$ in $\mathbf{A}_{4\times3}$ is up to a rotation matrix $\mathbf{R}$ (*i.e.*, $12 - 3 = 9$). Hence, nine load constraints are sufficient to find $\mathbf{q}$,

$$|\mathcal{C}|_{min} = 9 \tag{21}$$

which corresponds to the case $\text{rank}(\mathbf{L}) = 9$ in (18).

B. Gravity magnitude constraint

From Definition 1, a load constraint set that is solely composed of the gravity magnitude is $\mathcal{C}_{\tau=1}^*$. The following lemmas provide analytic tools to investigate the rank of $\mathbf{L}$.

Definition 2. $\text{rank}(\mathbf{L}|\widehat{\mathbf{F}}_b, \mathcal{C})$ *is the rank of* $\mathbf{L}$ *when* $\widehat{\mathbf{F}}_b$ *and* $\mathcal{C}$ *are given for the construction of* $\mathbf{L}$ *in* (14).

Lemma 1. $\text{rank}(\mathbf{L}|\widehat{\mathbf{F}}_b, \mathcal{C}) = \text{rank}(\mathbf{L}|\mathbf{F}_b, \mathcal{C})$ *for any* $\mathcal{C}$.

Lemma 2. $\text{rank}(\mathbf{L}|\widehat{\mathbf{F}}_b, \mathcal{C}) = \min\{10,\ \text{rank}(\mathcal{S}[\mathbf{f}_{b,i} \otimes \mathbf{f}_{b,j}])\}$

Proof: (for Lemma 1 and 2) From (7), $\mathbf{f}_{b,i} = \mathbf{A}_{4\times4}^\top \widehat{\mathbf{f}}_{b,i}$. The mixed-product and transpose property of the Kronecker product [29] rewrite $\mathbf{L}$ in (13) as follows:

$$\mathbf{L}(\widehat{\mathbf{F}}_b, \mathcal{C}) = \mathcal{S}[\widehat{\mathbf{f}}_{b,i} \otimes \widehat{\mathbf{f}}_{b,j}]^\top \mathbf{T}_{16\times10} \tag{22}$$

$$= \mathcal{S}[\mathbf{f}_{b,i} \otimes \mathbf{f}_{b,j}]^\top (\mathbf{A}_{4\times4} \otimes \mathbf{A}_{4\times4})^\top \mathbf{T}_{16\times10}, \tag{23}$$

$$\mathbf{L}(\mathbf{F}_b, \mathcal{C}) = \mathcal{S}[\mathbf{f}_{b,i} \otimes \mathbf{f}_{b,j}]^\top \mathbf{T}_{16\times10} \tag{24}$$

Based on $\text{rank}(\mathbf{XY}) \leq \min\{\text{rank}(\mathbf{X}), \text{rank}(\mathbf{Y})\}$, $\mathbf{L}$ has the same rank for $\widehat{\mathbf{F}}_b$ and $\mathbf{F}_b$ since $\text{rank}(\mathbf{A}_{4\times4} \otimes \mathbf{A}_{4\times4}) = 16$ and $\text{rank}(\mathbf{T}_{16\times10}) = 10$ from an invertible $\mathbf{A}_{4\times4}$ and $\mathbf{T}_{16\times10}$ in Appendix A. Lemma 2 is proven by the same rank property from (24). ∎

Lemma 1 and 2 enable us to analyze the rank of the linear system $\mathbf{L}(\widehat{\mathbf{F}}_b, \mathcal{C})$ through a true $\mathbf{F}_b$ instead of $\widehat{\mathbf{F}}_b$. When $\mathcal{C} = \mathcal{C}_{\tau=1}^*$, $\mathbf{L}$ has the following properties:

TABLE I. Solution schemes for a redundant IMU according to $\text{rank}(\mathbf{L})$

$\text{rank}(\mathbf{L})$	solution for $\mathbf{q}$ and examples
< 9	$\mathbf{q}$ is indeterminate ex) lack of load constraints: $|\mathcal{C}| < |\mathcal{C}|_{min} = 9$. ex) degenerate load configuration $\mathbf{F} \in \mathcal{D}_\mathbf{F}$ in Fig. 7.
9	$\mathbf{q} = \mathbf{L}^+\mathbf{c} + \alpha\mathbf{q}_n,\ \mathbf{q}_n \in \mathcal{N}(\mathbf{L})$ determine α using q-constraint (16) ex) minimal constraints: $|\mathcal{C}| = 9$ ex) gravity magnitudes: $\mathcal{C} = \mathcal{C}_{\tau=1}^*$ s.t. $|\mathcal{C}^*| \geq 9$
10	$\mathbf{q} = \mathbf{L}^+\mathbf{c}$ for noisy $\mathbf{Z}$, enforce $\text{rank}(\mathbf{Q}) = 3$ using SVD ex) non-minimum mixed constraint: $\mathcal{C} - \mathcal{C}^* \neq \emptyset$ ex) various magnitudes: $\mathcal{C} = (\mathcal{C}^* - \mathcal{C}_{\tau=1}^*)$

$|\mathcal{C}|$ denotes the number of constraints in $\mathcal{C}$.

Proposition 1. *When* $\mathcal{C} = \mathcal{C}_{\tau=1}^*$, $\text{rank}(\mathbf{L}) \leq 9$.

Proof: Let $\mathbf{f}_i = [x_i, y_i, z_i]^\top$. The column expansion of the matrix $\mathcal{S}[\mathbf{f}_{b,i}^\top \otimes \mathbf{f}_{b,i}^\top]$ with $\mathbf{f}_{b,i}^\top = [\mathbf{f}_i^\top\ 1]$ shows that six duplicated columns exist in (25) and thus the maximum rank is bounded to 10 as seen in (26).

$$\text{rank}(\mathcal{S}[\mathbf{f}_{b,i}^\top \otimes \mathbf{f}_{b,i}^\top]) = \text{rank}(\mathcal{S}[(\mathbf{f}_i \otimes \mathbf{f}_i)^\top\ \mathbf{f}_i^\top\ \mathbf{f}_i^\top\ 1]) \tag{25}$$

$$= \text{rank}(\mathcal{S}[(\mathbf{f}_i \otimes \mathbf{f}_i)^\top\ 1]) \tag{26}$$

$$= \text{rank}(\mathcal{S}[x_i^2\ y_i^2\ z_i^2\ x_iy_i\ y_iz_i\ z_ix_i\ x_i\ y_i\ z_i\ 1]) \tag{27}$$

$$= \text{rank}(\mathcal{S}[x_i^2\ y_i^2\ z_i^2\ x_iy_i\ y_iz_i\ z_ix_i\ x_i\ y_i\ z_i]) \tag{28}$$

$$\leq 9 \tag{29}$$

Since $\mathbf{f}_i$ in $\mathcal{C}_{\tau=1}^*$ are subject to $x_i^2 + y_i^2 + z_i^2 - 1 = 0$ for all i, the first three columns and the last column in (27) are linearly dependent and thus their maximum rank decreases by one. From Lemma 2, $\text{rank}(\mathbf{L}) \leq 9$ for $\mathcal{C}_{\tau=1}^*$. ∎

Proposition 2. *When* $\mathcal{C} = \mathcal{C}_{\tau=1}^*$, *only one root of* $f(\alpha)$ *satisfies the q-constraint.*

Proof: $\mathbf{Q} = \mathbf{A}_{4\times3}\mathbf{A}_{4\times3}^\top = \mathbf{A}_{4\times4}\,\text{diag}(1,1,1,0)\,\mathbf{A}_{4\times4}^\top$ from (12). Suppose $\mathbf{A}_{4\times4} = \mathbf{I}$. From $\widehat{\mathbf{f}}_{b,i} = \mathbf{f}_{b,i} = [x_i\ y_i\ z_i\ 1]^\top$ and $\mathcal{C}_{\tau=1}^*$ $(x_i^2 + y_i^2 + z_i^2 - 1 = 0$ for all $i)$, a linear system $\mathbf{Lq} = \mathbf{1}$ is satisfied by the following particular and null solutions:

$$\mathbf{L} = \mathcal{S}[x_i^2\ 2x_iy_i\ 2z_ix_i\ 2x_i\ y_i^2\ 2y_iz_i\ 2y_i\ z_i^2\ 2z_i\ 1] \tag{30}$$

$$\mathbf{q}_p = \frac{1}{4}[\,1\ 0\ 0\ 0\ 1\ 0\ 0\ 1\ 0\ 3\,]^\top \tag{31}$$

$$\mathbf{q}_n = \frac{1}{2}[\,1\ 0\ 0\ 0\ 1\ 0\ 0\ 1\ 0\ \text{-}1\,]^\top \tag{32}$$

Then, $\mathbf{q} = \mathbf{q}_p + \alpha\mathbf{q}_n$ is equal to a symmetric matrix $\mathbf{Q}$ s.t.

$$\mathbf{Q} = \begin{bmatrix} q_1 & & & \\ q_2 & q_5 & & \\ q_3 & q_6 & q_8 & \\ q_4 & q_7 & q_9 & q_{10} \end{bmatrix} = \frac{1}{4}\begin{bmatrix} 1+2\alpha & & & \\ 0 & 1+2\alpha & & \\ 0 & 0 & 1+2\alpha & \\ 0 & 0 & 0 & 3-2\alpha \end{bmatrix} \tag{33}$$

The rank condition of the q-constraint yields $\det(\mathbf{Q}) = f(\alpha) = (1 + 2\alpha)^3(3 - 2\alpha) = 0$, which has two real roots, $\alpha = 1.5$ or -0.5. Only $\alpha = 1.5$ is true because $\alpha = -0.5$ cannot produce a positive definite $\mathbf{Q}_{3\times3}$. This uniqueness of
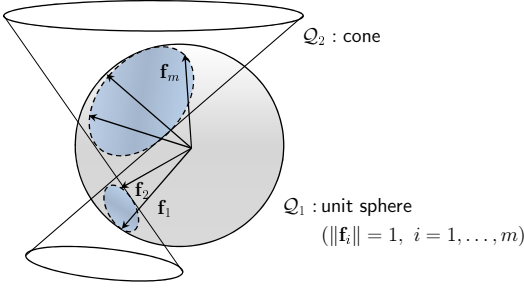
Fig. 6. Degenerate condition of calibration load set $\mathbf{F}$ in $\mathcal{C}_{\tau=1}^*$: $\mathbf{F}$ is degenerate if $\mathbf{F} = (\mathbf{f}_1, \ldots, \mathbf{f}_m)$ lies on the intersection of $\mathcal{Q}_1$ (sphere) and $\mathcal{Q}_2$ (any other quadric, *e.g.*, cone).
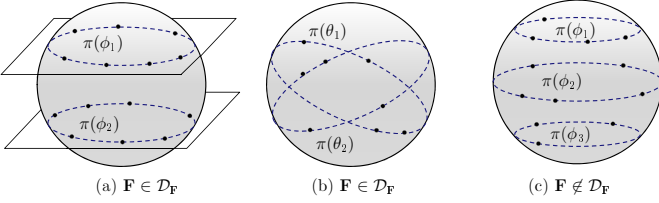

Fig. 7. Examples of degenerate and non-degenerate calibration load sets $\mathbf{F}$ in $\mathcal{C}_{\tau=1}^*$: (a) $\mathbf{F} \in \mathcal{D}_{\mathbf{F}}$ when $\mathbf{F}$ is on $\mathcal{Q}_2 : \pi(\phi_1)\pi(\phi_2)$ generated by two discrete roll angles ϕ, (b) $\mathbf{F} \in \mathcal{D}_{\mathbf{F}}$ when $\mathbf{F}$ is on $\mathcal{Q}_2 : \pi(\theta_1)\pi(\theta_2)$ generated by two discrete pitch angles θ, (c) $\mathbf{F} \notin \mathcal{D}_F$ when $\mathbf{F}$ is on a non-quadric $\pi(\phi_1)\pi(\phi_2)\pi(\phi_3)$ generated by three discrete roll angles.

α satisfying the q-constraint is invariant to the multiplication of $\mathbf{Q}$ by any invertible matrix $\mathbf{A}_{4\times4}$. ∎

Regardless of the number of measurements ($m \geq |\mathcal{C}|_{min}$) that are collected in $\mathbf{Z}$, Proposition 1 and 2 claim that the accelerometer calibration based on gravity magnitude should take a one-dimensional null space of $\mathbf{L}$ into account and have a unique reconstruction for $\mathbf{S}_b$.

C. Degenerate load configuration

Proposition 1 shows a case where a particular load constraint set produces a null space in $\mathbf{L}$. We also investigate a case when a particular geometric distribution of loads $(\mathbf{f}_1, \ldots, \mathbf{f}_m)$ causes a null space $\mathcal{N}(\mathbf{L})$. If the dimension of a null-space is greater than one, *i.e.*, rank$(\mathbf{L}) < 9$, the linear system $\mathbf{L}$ is unsolvable, leading to failure in factorization.

Definition 3. $\mathcal{D}_{\mathbf{F}}$ *is a degenerate set of calibration loads* $\mathbf{F} = (\mathbf{f}_1, \ldots, \mathbf{f}_m)$, *which becomes* rank$(\mathbf{L}|\mathbf{F}_b, \mathcal{C}) < 9$.

Proposition 3. *When* $\mathcal{C} = \mathcal{C}^*$, $\mathcal{N}(\mathbf{L}) \neq \emptyset$ *if and only if a calibration load set* $\mathbf{F} = (\mathbf{f}_1, \ldots, \mathbf{f}_m)$ *lies on a quadric* $\mathcal{Q}$, *i.e.*, $[\mathbf{f}_i^\top 1]\mathcal{Q}[\mathbf{f}_i^\top 1]^\top = 0$ *for* $i = 1, \ldots, m$.

Proof: Let $\mathbf{L}_\mathcal{S} = \mathcal{S}[(\mathbf{f}_i \otimes \mathbf{f}_i)^\top \quad 1])$ be the stacked matrix as seen in (27). $\mathcal{N}(\mathbf{L})$ is not empty if and only if a non-zero $\mathbf{a}$ exists such that $\mathbf{L}_\mathcal{S}\mathbf{a} = \mathbf{0}$. Given $\mathcal{C}^*$, $\mathbf{a}$ can be represented by a quadric $\mathcal{Q}$: $\mathcal{Q}$ is a symmetric matrix in $\mathcal{R}^{4\times4}$ and $\mathbf{f}_{b,i}^\top \mathcal{Q}(\mathbf{a}) \mathbf{f}_{b,i} = 0$, *i.e.*, $a_0 x_i^2 + a_1 y_i^2 + a_2 z_i^2 + a_3 x_i y_i + a_4 y_i z_i + a_5 z_i x_i + a_6 x_i + a_7 y_i + a_8 z_i + a_9 = 0$ for all i. Hence, a non-empty $\mathcal{N}(\mathbf{L})$ is equivalent to the existence of a quadric $\mathcal{Q}$ on which $\mathbf{F}$ lies. ∎

Proposition 4. *When* $\mathcal{C} = \mathcal{C}_{\tau=1}^*$, $\mathbf{F} \in \mathcal{D}_{\mathbf{F}}$ *if and only if* $\mathbf{F} = (\mathbf{f}_1, \ldots, \mathbf{f}_m)$ *lies on a non-sphere quadric* $\mathcal{Q}_2$.

Proof: The degeneracy condition, rank$(\mathbf{L}) < 9$, occurs when at least two linearly independent vectors $(\mathbf{a}_1, \mathbf{a}_2, \ldots)$ exist such that $\mathbf{L}_\mathcal{S}\mathbf{a}_1 = \mathbf{L}_\mathcal{S}\mathbf{a}_2 = \cdots = \mathbf{0}$. Proposition 1 shows that $\mathcal{C}_{\tau=1}^*$ already has $\mathbf{a}_1 = [1\ 1\ 1\ 0\ 0\ 0\ 0\ 0\ 0\ \text{-}1]^\top$, which is a unit sphere $\mathcal{Q}_1 : x_i^2 + y_i^2 + z_i^2 - 1 = 0$. Thus, $\mathbf{a}_2$ represents another quadric $\mathcal{Q}_2$, which is not a unit sphere. ∎

Based on Proposition 3, we see that geometric properties in $\mathcal{D}_{\mathbf{F}}$ for an intra-relation constraint $\mathcal{C}^*$ can be analyzed via 3D quadric fitting. The dimension η of $\mathcal{N}(\mathbf{L})$ is equal to the number of quadrics $(\mathcal{Q}_1, \ldots, \mathcal{Q}_\eta)$ that can represent $\mathbf{F}$ simultaneously. For example, $\mathcal{C}_{\tau=1}^*$ has $\eta = 2$ when the loads in $\mathbf{F} \in \mathcal{D}_{\mathbf{F}}^*$ are distributed at the intersection of a unit sphere $\mathcal{Q}_1$ and any other quadric $\mathcal{Q}_2$ as in Fig. 6. In essence, $\mathcal{D}_{\mathbf{F}}$ in $\mathcal{C}_{\tau=1}^*$ is determined based on whether another possible quadric fitting of $\mathbf{F}$ exists other than the original constraint (geometrically a unit sphere) as shown the following remarks:

Remark 1. *When* $\mathcal{C} = \mathcal{C}_{\tau=1}^*$, $\mathbf{F} \in \mathcal{D}_{\mathbf{F}}$ *if* $\mathbf{F}$ *lies on one or two cutting planes of a unit sphere.*

Remark 2. *When* $\mathcal{C} = \mathcal{C}_{\tau=1}^*$, $\mathbf{F} \notin \mathcal{D}_{\mathbf{F}}$ *if* $\mathbf{F}$ *lies on three and more cutting planes of a unit sphere.*

If loads in $\mathbf{F}$ are distributed on two planes like Fig. 7(a-b), they lie on $\boldsymbol{\pi} = \boldsymbol{\pi}_1\boldsymbol{\pi}_2 = (a_1 x_i + b_1 y_i + c_1 z_i + d_1)(a_2 x_i + b_2 y_i + c_2 z_i + d_2) = 0$. By Proposition 4, $\mathbf{F}$ is degenerate because $\boldsymbol{\pi}$ is able to represent a non-sphere quadric $\mathcal{Q}_2$. In contrast, if $\mathbf{F}$ is distributed on more than two planes like Fig. 7(c), it is not degenerate because a unit sphere $\mathcal{Q}_1$ is the only quadric which $\mathbf{F}$ lies on. The cubic polynomial ($\prod_{i=1}^{n\geq3} \boldsymbol{\pi}_i = 0$) cannot be represented by a quadric.

When an IMU is randomly oriented manually in the calibration, it is far less likely that $\mathbf{F}$ forms a non-sphere quadric. However, special attention should be paid when pivotal devices such as a tripod are used. More specifically, one should make sure to generate at least three roll or pitch angles during measurement collection.

VII. TRIAD IMU CALIBRATION

The factorization method allows the shape parameter dimension (p) up to the number of components (n). For a triad IMU ($n = 3$), the exclusion of the bias from $\mathbf{S}_b$ reduces the parameter dimension to $p = 3$ in $\mathbf{S}$. The bias is iteratively estimated outside of the factorization loop using motion reconstruction errors compared with a load constraint $\mathcal{C}$. Note that the following iterative algorithm is specific to $\mathcal{C}^*$.

A. Iterative algorithm

Let $\mathbf{D}$ denote bias-compensated measurements in which the bias is subtracted from $\mathbf{Z}$ in (2):

$$\mathbf{D} = \begin{bmatrix} \mathbf{f}_1^\top \mathbf{s}_1 & \mathbf{f}_1^\top \mathbf{s}_2 & \cdots & \mathbf{f}_1^\top \mathbf{s}_n \\ \vdots & \vdots & & \vdots \\ \mathbf{f}_m^\top \mathbf{s}_1 & \mathbf{f}_m^\top \mathbf{s}_2 & \cdots & \mathbf{f}_m^\top \mathbf{s}_n \end{bmatrix} = \mathbf{F}\mathbf{S} \quad (34)$$

A bilinear formulation of $\mathbf{D}$ is the product of two matrices, $\mathbf{F}$ and $\mathbf{S}$, and $\text{rank}(\mathbf{D}) = 3$. The constraints used for the factorization are identical with those for a redundant IMU except that $\mathbf{D}$ is used instead of $\mathbf{Z}$.

Suppose that an initial bias $\mathbf{b}^0$ is given. At the k-th iteration, the proper rank constraint ($p = 3$) on $\mathbf{D}^k$ yields

$$\mathbf{D}^k = \mathbf{Z} - \mathbf{1}_{m \times 1} \mathbf{b}^k \tag{35}$$

$$= (\widehat{\mathbf{F}} \mathbf{A}_{3 \times 3})(\mathbf{A}_{3 \times 3}^{-1} \widehat{\mathbf{S}}) \tag{36}$$

from $\text{svd}(\mathbf{D}^k) = \mathbf{U}\boldsymbol{\Sigma}\mathbf{V}^\top$, $\widehat{\mathbf{F}} = \mathbf{U}\boldsymbol{\Sigma}^{1/2}$ and $\widehat{\mathbf{S}} = \boldsymbol{\Sigma}^{1/2}\mathbf{V}^\top$. True shape and motion matrices are now indeterminate up to an invertible matrix $\mathbf{A}_{3 \times 3}$. From $\mathbf{f}_i = \mathbf{A}_{3 \times 3}^\top \widehat{\mathbf{f}}_i$, each load constraint in $\mathcal{C}^*$ produces one linear equation for $\mathbf{q}'$:

$$c_{ii} = \widehat{\mathbf{f}}_i^\top (\mathbf{A}_{3 \times 3} \mathbf{A}_{3 \times 3}^\top) \widehat{\mathbf{f}}_i = \widehat{\mathbf{f}}_i^\top \mathbf{Q}_{3 \times 3} \widehat{\mathbf{f}}_i \tag{37}$$

$$= [\widehat{\mathbf{f}}_i \otimes \widehat{\mathbf{f}}_j]^\top \mathbf{T}_{9 \times 6} \, \mathbf{q}' \tag{38}$$

where $\mathbf{q}' \in \mathcal{R}^{6 \times 1}$ is a vector of lower triangular elements of a symmetric matrix $\mathbf{Q}_{3 \times 3}$, and $\mathbf{T}_{9 \times 6}$ is a constant conversion matrix from a vectorized $\mathbf{Q}_{3 \times 3}$ to $\mathbf{q}'$ (see Appendix A). Then, $\mathbf{q}'$ can be found from the following linear system equation:

$$\mathbf{L}' \mathbf{q}' = \mathbf{c} \tag{39}$$

where $\mathbf{L}' = \mathcal{S}[\widehat{\mathbf{f}}_i \otimes \widehat{\mathbf{f}}_i]^\top \mathbf{T}_{9 \times 6}$. Note that $\mathbf{q}'$ is solvable only if $\mathbf{L}'$ has a full rank because $\mathbf{q}'$ has no internal constraints like the rank condition of the q-constraint in (16a). Then, the factorization is completed via the Cholesky decomposition of $\mathbf{Q}_{3 \times 3}$ into $\mathbf{A}_{3 \times 3}$. The best reconstruction at the k-th step is given as $\mathbf{F}^k = \widehat{\mathbf{F}} \mathbf{A}_{3 \times 3}$ and $\mathbf{S}^k = \mathbf{A}_{3 \times 3}^{-1} \widehat{\mathbf{S}}$.

Since $\mathbf{D}^k$ is incompletely compensated due to the bias error in $\mathbf{b}^k$, we update a new bias $\mathbf{b}^{k+1}$ for the next iteration as

$$\overline{\mathbf{f}}_i = \frac{\sqrt{c_{ii}}}{\|\mathbf{f}_i^k\|} \mathbf{f}_i^k, \quad i = 1, \ldots, m \tag{40}$$

$$\mathbf{S}_b = [\overline{\mathbf{F}} \; \mathbf{1}]^+ \mathbf{Z} \tag{41}$$

$$\mathbf{b}^{k+1} = \texttt{last-row}(\mathbf{S}_b). \tag{42}$$

and the iteration continues until $\|\mathbf{b}^{k+1} - \mathbf{b}^k\| < \varepsilon$ for a given termination threshold ε.

Since the bias residual in $\mathbf{b}^k$ contaminates $\mathbf{D}^k$, the reconstructed motion and shape matrices, $\mathbf{F}^k$ and $\mathbf{S}^k$, are also incorrect. The least squares solution $\mathbf{q}'$ in (39) has a residual that leaves $\mathbf{F}^k$ incompletely constrained by $\mathcal{C}^*$. Hence, each load constraint in $\mathcal{C}^*$ is explicitly re-enforced on the reconstructed motion $\mathbf{F}^k$ in order to find an improved bias. In other words, the magnitude of each motion $\mathbf{f}_i^k$ is normalized to $\|\mathbf{f}_i^k\|^2 = c_{ii}$. Then, a new bias $\mathbf{b}^{k+1}$ for the next iteration is computed from the updated $\mathbf{F}^k$ and the measurement $\mathbf{Z}$.

B. Convergence region

Advantages of this iterative factorization over nonlinear methods [13]–[15] includes its requirement for just an initial bias. There is no need to presume initial values of scale factors and alignments.

Convergence of the bias is demonstrated to be insusceptible to initial bias error. The simulation and experiments in Fig. 11

Algorithm 2: Triad IMU calibration using $\mathcal{C}^*$ ($n = 3$)

Input: $\mathbf{Z}$, $\mathcal{C}^*$, $\mathbf{b}^0$, ε,   Output: $\mathbf{S}_b$
$p = 3$, $k = 0$
repeat
  $[\mathbf{U}, \mathbf{S}, \mathbf{V}] = \texttt{svd}(\mathbf{Z} - \mathbf{b}^k)$
  $\widehat{\mathbf{F}} = \mathbf{U}_p \boldsymbol{\Sigma}_p^{1/2}$, $\widehat{\mathbf{S}} = \boldsymbol{\Sigma}_p^{1/2} \mathbf{V}_p^\top$
  foreach c_{ii} in $\mathcal{C}$ **do**
    $\mathbf{L}_i' = [\widehat{\mathbf{f}}_{b,i} \otimes \widehat{\mathbf{f}}_{b,i}]^\top \mathbf{T}_{9 \times 6}$
  $\mathbf{q}' = \mathbf{L}'^+ \mathbf{c}$, $\mathbf{Q}_{3 \times 3} = \texttt{convert}(\mathbf{q}')$
  $\mathbf{A}_{3 \times 3} = \texttt{chol}(\mathbf{Q}_{3 \times 3})$
  $\mathbf{S} = \mathbf{A}_{3 \times 3}^{-1} \widehat{\mathbf{S}}$, $\mathbf{F} = \widehat{\mathbf{F}} \mathbf{A}_{3 \times 3}$
  foreach $\mathbf{f}_i$ in $\mathbf{F}$ **do**
    $\overline{\mathbf{f}}_i = (\sqrt{c_{ii}}/\|\mathbf{f}_i\|) \mathbf{f}_i$
  $\mathbf{S}_b = [\overline{\mathbf{F}} \; \mathbf{1}]^+ \mathbf{Z}$
  $\mathbf{b}^{k+1} = \texttt{last-row}(\mathbf{S}_b)$
  $k \leftarrow k + 1$
until $\|\mathbf{b}^{k+1} - \mathbf{b}^k\| < \varepsilon$

---

and 16 show that the convergence region is wide enough to cover $\|\mathbf{b}^0 - \mathbf{b}^*\| < \|\mathbf{s}\|$ (when $\|\mathbf{f}\| = 1$) for a true bias $\mathbf{b}^*$. When $\mathbf{Z}$ is generated by $\mathcal{C}_{\tau=1}^*$, one automatic setting for each initial bias would be $\mathbf{b}^0 = \text{mean}(\mathbf{Z})$ because no measurements are greater than a scale factor from the bias.

VIII. PERFORMANCE EVALUATION

The performance of factorization-based IMU calibration is evaluated mainly for an accelerometer unit under the gravity magnitude constraint $\mathcal{C}_{\tau=1}^*$ in Fig. 3. In the following numerical simulations, a true shape $\mathbf{S}_b$ has a unit scale factor and unit bias, $\|\mathbf{s}_i\| = b_i = 1$ for $i = 1, \ldots, n$, and consists of multiple tri-axial units while each unit is skewed to each other.

A. Numerical example

The following is an example of measurements collected into $\mathbf{Z}$, with the absence of measurement noise, from a four-component accelerometer unit and ten different attitudes in static conditions ($n = 4, m = 10$). From the SVD of the $\mathbf{Z}$ with $\text{rank}(\mathbf{Z}) = 4$, $\widehat{\mathbf{F}}_b$ and $\widehat{\mathbf{S}}_b$ are computed as

$$\mathbf{Z} = \begin{bmatrix} 0.134 & 1.433 & 0.750 & 1.393 \\ 0.134 & 0.567 & 0.750 & 1.826 \\ 0.412 & 1.000 & 0.191 & 1.866 \\ 0.792 & 1.847 & 0.511 & 1.026 \\ 0.792 & 0.153 & 0.511 & 1.873 \\ 1.208 & 1.847 & 0.511 & 0.818 \\ 1.208 & 1.000 & 0.022 & 1.588 \\ 1.588 & 1.701 & 0.595 & 0.642 \\ 1.588 & 0.299 & 0.595 & 1.342 \\ 1.866 & 1.000 & 0.500 & 0.921 \end{bmatrix}$$

$$= \underbrace{\begin{bmatrix} -0.75 & 0.22 & 0.64 & -0.26 \\ -0.67 & 0.71 & 0.21 & -0.32 \\ -0.78 & 0.49 & 0.24 & 0.40 \\ -0.86 & -0.30 & 0.48 & 0.03 \\ -0.70 & 0.66 & -0.38 & -0.08 \\ -0.88 & -0.53 & 0.26 & 0.01 \\ -0.85 & 0.11 & -0.20 & 0.57 \\ -0.89 & -0.68 & -0.02 & -0.13 \\ -0.76 & 0.11 & -0.73 & -0.23 \\ -0.85 & -0.41 & -0.53 & -0.08 \end{bmatrix}}_{\widehat{\mathbf{F}}_b} \underbrace{\begin{bmatrix} -1.25 & -1.40 & -0.60 & -1.61 \\ -0.68 & -0.72 & 0.08 & 1.13 \\ -1.00 & 0.90 & 0.09 & -0.04 \\ 0.04 & 0.13 & -0.84 & 0.17 \end{bmatrix}}_{\widehat{\mathbf{S}}_b}$$

TABLE II. Calibration performance for $\mathcal{C}^*_{\tau=1}$ with respect to noise (σ) and component size (n) (simulation)

σ (%)	bias ($\mathbf{b}_{err}$, %)			scale ($\|\mathbf{s}\|_{err}$, %)			alignment ($\angle \mathbf{s}_1 \mathbf{s}_{i,err}$, deg)		
	$n=4$	$n=6$	$n=20$	$n=4$	$n=6$	$n=20$	$n=4$	$n=6$	$n=20$
0.25	-0.01 ± 0.82	-0.01 ± 0.56	0.00 ± 0.31	-0.02 ± 0.84	-0.01 ± 0.59	0.00 ± 0.32	0.00 ± 0.42	0.00 ± 0.22	0.00 ± 0.12
0.5	0.02 ± 1.67	0.01 ± 1.11	0.01 ± 0.60	0.09 ± 1.72	0.04 ± 1.16	0.02 ± 0.63	0.00 ± 0.83	0.00 ± 0.44	0.00 ± 0.23
1.0	0.23 ± 3.53	-0.01 ± 2.17	-0.03 ± 1.31	0.66 ± 3.54	-0.04 ± 2.27	-0.07 ± 1.37	0.01 ± 1.75	0.01 ± 0.86	0.00 ± 0.48
4.0	2.24 ± 27.0	-0.03 ± 10.9	-0.58 ± 5.30	7.43 ± 27.0	0.27 ± 11.4	-1.55 ± 5.33	0.03 ± 8.04	-0.01 ± 3.58	-0.04 ± 1.95
8.0	1.58 ± 45.6	-0.10 ± 23.3	-2.27 ± 13.0	11.1 ± 46.3	1.04 ± 24.2	-5.88 ± 12.1	-0.20 ± 14.8	-0.10 ± 7.21	-0.18 ± 4.36

The load size is fixed to 36 ($m = 36$). See Figure 8 for the plot.

From $\mathcal{C}^*_{\tau=1}$, $\mathbf{L}$ has a one-dimensional null space. The corresponding solutions for $\mathbf{q}$ and α are

$$
\mathbf{q}_p = \begin{bmatrix} 1.28 \\ -0.15 \\ -0.01 \\ 0.00 \\ 0.39 \\ 0.01 \\ -0.09 \\ 0.42 \\ 0.00 \\ 0.15 \end{bmatrix}, \quad
\mathbf{q}_n = \begin{bmatrix} 0.40 \\ -0.11 \\ 0.03 \\ 0.23 \\ -0.55 \\ -0.01 \\ 0.10 \\ -0.65 \\ 0.00 \\ -0.21 \end{bmatrix}, \quad
\alpha = \begin{pmatrix} 0.65 \\ 0.65 \\ 0.65 \\ -2.14 \end{pmatrix}
$$

Since only $\alpha = -2.14$ satisfies the q-constraint (16), the true $\mathbf{S}_b$ and $\mathbf{F}_b$ are recovered as

$$
\mathbf{A}_{4\times4} = \begin{bmatrix} 0.65 & 0 & 0 & -1.24 \\ 0.13 & 1.24 & 0 & 0.18 \\ -0.11 & 0.03 & 1.34 & -0.01 \\ -0.76 & -0.17 & -0.05 & -0.12 \end{bmatrix}
$$

$$
\mathbf{S}_b = \begin{bmatrix} 1 & 0 & 0 & -0.50 \\ 0 & 1 & 0 & -0.50 \\ 0 & 0 & 1 & -0.71 \\ 1 & 1 & 1 & & 1 \end{bmatrix}, \quad
\mathbf{F}_b = \begin{bmatrix} -0.87 & 0.43 & -0.25 & 1 \\ -0.87 & -0.43 & -0.25 & 1 \\ \vdots & \vdots & \vdots & \vdots \\ 0.59 & 0.70 & -0.40 & 1 \\ 0.59 & -0.70 & -0.40 & 1 \\ 0.87 & 0.00 & -0.50 & 1 \end{bmatrix}
$$

B. Performance of gravity magnitude constraint

The performance of accelerometer calibration in $\mathcal{C}^*_{\tau=1}$ was assessed through simulation in terms of the following three factors: Gaussian measurement noise (σ), number of loads (load size $m = |\mathcal{C}^*_{\tau=1}|$), and number of sensor components (component size n). In order to reflect a true scenario in in-field calibration, the IMU's attitude (roll and pitch) was randomly selected but bounded within ± 60 degrees. Gaussian noise σ was given as a percentage of the scale factor $\|\mathbf{s}_i\|$.

For every triplet (σ, m, n), a Monte-Carlo simulation was performed with 1000 trials. From Fig. 8 to 10, the bias and scale factor error were evaluated for every sensor component and alignment error was evaluated using vector angles of all possible pairs of sensor components.

Fig. 8 and 9 show that calibration error decreases linearly as component size (n) increases from 4 to 24, load size (m) increases from 9 to 144, or as measurement noise (σ) decreases from 8 to 0.25%. Table II shows the errors in more details and indicates that the factorization method is an unbiased estimator unless the measurement noise becomes too severe ($\sigma \geq 4.0\%$).

Fig. 10 shows a case where angular motion constraints (inter-relation constraint) and $\mathcal{C}^*_{\tau=1}$ (intra-relation constraint) are used together. Half of the constraints are given as $\mathbf{f}_i^\top \mathbf{f}_j = 0$ from multiple pairs of orthogonal loads [18]. Compared with
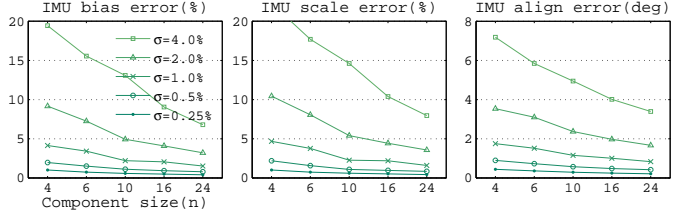

Fig. 8. IMU calibration performance with respect to component size (n) and noise (σ) when the gravity magnitude constraint $\mathcal{C}^*_{\tau=1}$ is used.
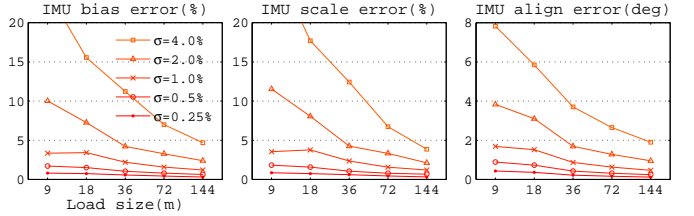

Fig. 9. IMU calibration performance with respect to load size (m) and noise (σ) when the gravity magnitude constraint $\mathcal{C}^*_{\tau=1}$ is used.
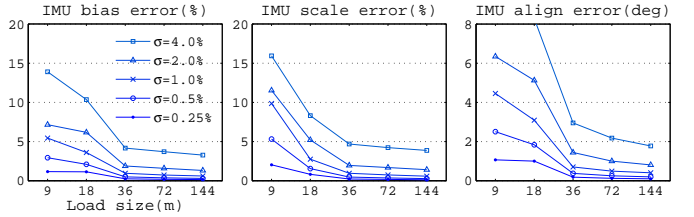

Fig. 10. IMU calibration performance of mixed constraint types when the gravity magnitude constraint $\mathcal{C}^*_{\tau=1}$ (50%) and the orthogonal motion constraint (50%) are used together.

Fig. 9 that uses $\mathcal{C}^*_{\tau=1}$ only, the bias and scale factor error decrease almost half as load size increases while the alignment error is greater for a small m. This indicates that additional knowledge about angular relation constrains the bias and scale factor more when m is large.

Since a typical MEMS-based accelerometer [30] has a noise of less than $\sigma = 0.25\%$, the calibration result for an off-the-shelf IMU is expected to be better than 0.01% accuracy and 0.5% precision when $m = 30$ and $n = 6$. The minimal load and component size ($m = 9$, $n = 4$) have 0.02% accuracy and 0.8% precision when $\sigma = 0.25\%$.

Calibration failure occurs when no solution for $\mathbf{q}$ produces a positive definite $\mathbf{Q}_{3\times3}$ in (16), which is usually induced by high measurement noise. Table III shows the failure rate for 1000 trials in simulation when $\mathcal{C}^*_{\tau=1}$ is used. Failure begins to occur when the noise becomes larger than $\sigma = 2.0\%$ and is significantly reduced as the load and component size increases. In a practical sense, this failure would be little concern because
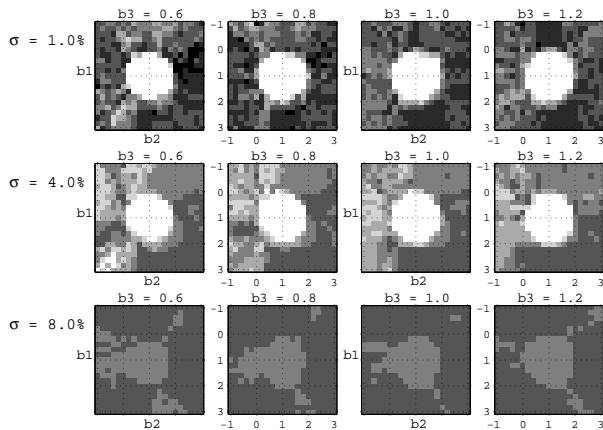
Fig. 11. Bias convergence region of the iterative factorization for a tri-axial IMU ($m = 10$ and $\mathcal{C}^*_{\tau=1}$). Each plot shows a cross section along b_3 and the rows correspond to 1.0, 4.0 and 8.0% noise level, respectively. The intensity indicates the percentage of bias convergence. Initial conditions, $\mathbf{b}^0 = [b_1\ b_2\ b_3]$, in the white region always converge to the true $\mathbf{b}^* = [1\ 1\ 1]$ while those in the black region always trap in local minima.
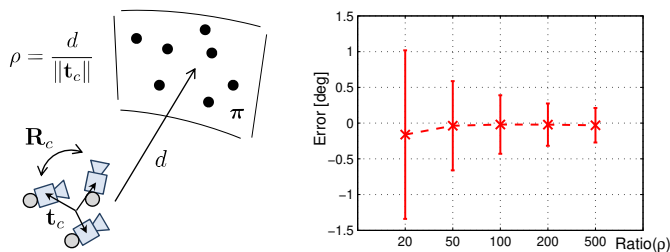

Fig. 12. Systematic error in camera rotation angle $\theta_c = \text{phase}(\text{eig}(\mathbf{H}))$ in terms of the distance ratio ρ. The homography $\mathbf{H}$ is estimated using image feature correspondence when the true θ_c is 10 degrees.

TABLE III. Failure rate (%) of the factorization method for a redundant IMU when $\mathcal{C}^*_{\tau=1}$ is used

noise (%)	$n = 4$	$n = 6$	$n = 10$	$n = 20$
0.5	0.0	0.0	0.0	0.0
1.0	0.0	0.0	0.0	0.0
2.0	0.2	0.0	0.0	0.0
4.0	9.6	6.7	1.4	0.0
8.0	31.3	30.4	18.4	6.2

the noise from a real accelerometer ($\sigma = 0.2\%$) typically corresponds to a zero failure rate.

C. Bias convergence region for a triad IMU

The iterative factorization for the triad IMU in Section VII requires an initial bias $\mathbf{b}^0$. In order to numerically evaluate its convergence region, we tested for every initial point between $\mathbf{b}^0_{min} = -[1\ 1\ 1]$ to $\mathbf{b}^0_{max} = [3\ 3\ 3]$ in a 0.1 resolution when a true shape is given as $\mathbf{b}^* = [1\ 1\ 1]$ and $\mathbf{S}^* = \mathbf{I}_{3\times3}$.

Fig. 11 shows the percentage of bias convergence obtained by running Monte Carlo simulation. Initial biases in the white region always converge to the true bias $\mathbf{b}^*$ but those in the black region always trap in local minima. For low to moderate noise level ($\sigma \leq 4.0\%$), a continuous convergence region $\mathcal{B}$ exists which spherically expands around the true bias. Since the radius of this central volume is at least one, we can

conclude that initial biases in $\|\mathbf{b}^0 - \mathbf{b}^*\| < 1$ all converges to a global minimum. In other words, initial error provided for the bias can be as large as 100% of the scale factor.

D. Homography angle for gyroscope calibration

In Fig. 4 and Section IV-C, θ_c has a systematic error in cases of non-zero camera translation ($\mathbf{t}_c \neq \mathbf{0}$) and finite scene points ($d \neq \infty$) due to the violation of a rotating camera. Let $\rho = d/\|\mathbf{t}_c\|$ denote a distance ratio between the distance d from the scene points and camera translation $\|\mathbf{t}_c\|$. A rotating camera assumption on θ_c is valid only if $\rho = \infty$. For a finite ρ, a systematic error of $\theta_c(\mathbf{H})$ is evaluated by the simulation as ρ increases from 10 to 500 in Fig. 12. The error is biased when $\rho < 100$ and its variance decreases logarithmically as ρ increases. When $\rho \geq 200$, the mean squared error of θ_c becomes less than 1%.

IX. EXPERIMENTS

A series of experiments on the factorization method was conducted using a low-cost small IMU/camera system, shown in Fig. 1 and 13. The redundant IMU ($n = 6$) was made of two tri-axial IMUs (O-Navi Gyrocube) which we aligned with a skewed angle. MEMS inertial components are Analog Devices' ADXL-203 and ADXRS-150 whose measuring ranges are $\pm 2g$ and $\pm 200\,°$/sec, respectively. A multi-channel 11-bit A/D converter sampled the output voltage at 100Hz. The Sentech CCD board camera captured 640×480 resolution images at 30 frames/sec.

All the experimental data sets of the IMU outputs and images tagged with timestamps are available online at `http://www.cs.cmu.edu/~myung/simCAL/data`.

A. Accelerometer self-calibration

To rapidly and reliably collect measurements subject to the gravity magnitude constraint $\mathcal{C}^*_{\tau=1}$, we placed the IMU on a tripod and oriented it within ± 60 degrees. Various attitudes were applied randomly but we made certain to have at least three different roll or pitch angles so as to prevent a degenerate load configuration $\mathcal{D}_{\mathbf{F}}$ like Fig. 7 (a-b).

Fig. 14 shows how the measurement matrix $\mathbf{Z}$ was collected from the output of six accelerometers during the tripod operation shown in Fig. 13. In total, four calibration datasets ($E1, \ldots, E4$) were generated with more than 20 loads, each at different times several days apart. The noise in $\mathbf{Z}$ was measured as 0.73, which corresponds to $\sigma = 0.2\%$ when scaled by an average scale factor ($\|\mathbf{s}\| = 365.0$).

Note that redundant calibration treats two tri-axial IMUs as a whole ($n = 6$) and triad calibration treats each tri-axial IMU individually ($n = 3$, $\mathbf{s}_{123}$ and $\mathbf{s}_{456}$). Table IV compares accelerometer parameters that were calibrated by these two methods, respectively, and shows little difference between them.

The estimation variance of calibration parameters over four experiments is plotted in Fig. 15. Deviations of the scale factor $\|\mathbf{s}_i\|$ and alignment $\angle \mathbf{s}_i \mathbf{s}_j$ for each component are less than 0.5% and $0.1°$, respectively. They are nearly same as the
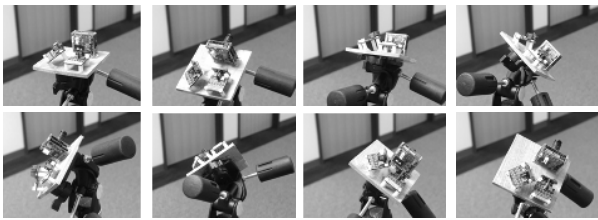
Fig. 13. The IMU placed on a tripod randomly oriented at various attitudes with respect to gravity.
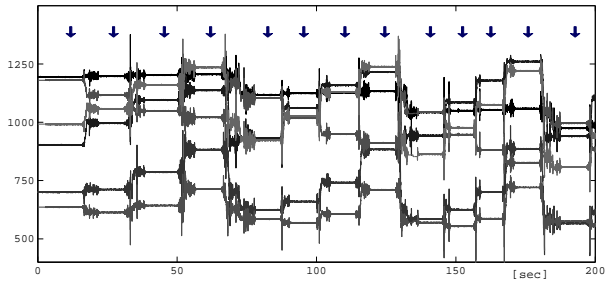

Fig. 14. The output of six accelerometers generated when the IMU is randomly oriented by a tripod. At each arrow in the plot, the output is collected into the measurement matrix $\mathbf{Z}$ when a static gravity is exerted on the accelerometers.

TABLE IV. Accelerometer calibration results from both redundant ($n = 6$) and triad ($n = 3$) calibration methods when $\mathcal{C}^*_{\tau=1}$. (Results are mainly shown for the first three components.)

No.	m	n	b_1	b_2	b_3	$\|\mathbf{s}_1\|$	$\|\mathbf{s}_2\|$	$\|\mathbf{s}_3\|$	$\angle\mathbf{s}_{12}$	$\angle\mathbf{s}_{13}$	$\angle\mathbf{s}_{14}$
E1	36	6	906.7	933.1	927.1	364.5	362.7	366.6	89.89	90.82	44.76
		3	906.5	933.6	926.8	364.3	362.2	366.3	89.85	90.85	–
E2	25	6	910.1	935.7	928.6	365.8	364.2	366.5	89.90	90.75	44.81
		3	909.7	935.7	927.8	365.7	363.9	365.8	89.91	90.82	–
E3	24	6	905.8	930.9	924.1	363.9	362.2	364.3	89.84	90.63	44.74
		3	905.6	930.9	922.3	363.4	361.7	362.4	89.82	90.68	–
E4	20	6	905.5	932.3	928.0	364.8	363.2	368.1	90.09	90.84	44.93
		3	905.4	932.2	922.9	362.5	361.7	362.8	90.06	90.92	–

Fig. 15. Estimation variance of accelerometer parameters: each parameter, individually obtained from four experiments, is compared using two methods, left (red) from the redundant calibration ($n = 6$) as a whole and right (blue) from the triad calibration ($n = 3$) of each tri-axial IMU in Fig. 1.

simulation evaluation (0.59% and $0.22°$ when $\sigma = 0.25\%$, $m = 36$ and $n = 6$ in Table II). The bias $\mathbf{b}$ show a relatively large deviation 1% since an operating temperature severely affects the bias of a MEMS component but was not maintained the same between the experiments.

An initial bias for the triad calibration was automatically provided as the mean of measurements, *i.e.*, $\mathbf{b}^0 = \mathrm{mean}(\mathbf{Z})$ and no convergence failure occurred in Table IV. The convergence rate in Fig. 16 shows that the bias asymptotically approaches to a steady state. For some initial condition, an overshoot is observed at the very beginning of the iteration. The convergence takes about 500 iterations when $\mathbf{b}^0$ is at a distance as far as 75% of the gravity magnitude.

Fig. 17 shows the accelerometer shape and motion matrix, $\mathbf{S}$ and $\mathbf{F}$, reconstructed by the factorization method. Each load in $\mathbf{F}$ that is located on a unit sphere reveals an applied attitude, and the shape of $\mathbf{S}$ recovers two tri-axial units arranged in a skewed angle.

B. Gyroscope self-calibration

Two sets of outdoor images (E5 and E6) in Fig. 18 were collected at different distances from the scene objects. The camera on a tripod was oscillated on diverse axes while the camera translation was limited to $\|\mathbf{t}_c\| < 0.1\mathrm{m}$. A far distance to the buildings ($d > 50\mathrm{m}$ for E5 and $d > 300\mathrm{m}$ for E6) validates the pure camera rotation assumption by $\rho \geq 500$.

Firstly, as shown in Fig. 19, we chose m peaks and filled the measurement $\mathbf{Z}$ with average gyroscope outputs $\mathbf{z}_i$ over camera frame intervals Δt_i closest to the peaks. The measurement noise was measured as 2.0 (equal to $\sigma = 0.66\%$ when scaled by $\|\mathbf{s}\| = 300$). Secondly, two neighboring images (I_i, I'_i) closest to each peak were chosen for the homography computation in Section IV-C. More than 200 feature points $\mathbf{x}_i$ were selected in I_i by the Harris corner detector [31] [32] and

Fig. 16. Convergence rate of the bias in the iterative linear calibration ($n = 3$) for the first three accelerometer components in the E4 experiment. Initial bias $\mathbf{b}^0 = [1100\ 1100\ 1100]$ (left) or $\mathbf{b}^0 = \mathrm{mean}(\mathbf{Z})$ (right).

Fig. 17. The accelerometer's shape and motion matrix ($\mathbf{F}$ and $\mathbf{S}$) reconstructed from the factorization-based redundant calibration ($n = 6$) in E4 experiment. All the gravity loads are located on a unit sphere. The two tri-axial IMUs are $(\mathbf{s}_1, \mathbf{s}_2, \mathbf{s}_3)$ and $(\mathbf{s}_4, \mathbf{s}_5, \mathbf{s}_6)$.

then tracked to $\mathbf{x}'_i$ in I'_i by KLT tracker [33] [34]. Given feature correspondence $(\mathbf{x}_i, \mathbf{x}'_i)$, the homography $\mathbf{H}_i$ such that $\mathbf{x}'_i = \mathbf{H}_i\mathbf{x}_i$ was found based on RANSAC to remove outliers [20]. Finally, the angular speed $\|\boldsymbol{\omega}_i\| = \theta_i/\Delta t_i$ was obtained from $\theta_i = \mathrm{phase}(\mathrm{eig}(\mathbf{H}_i))$ and $\Delta t_i = 1/30\mathrm{s}$. These m angular speeds

TABLE V. Gyroscope calibration results from the redundant ($n = 6$) and triad ($n = 3$) calibration methods when $\mathcal{C}^*$ is given by image feature tracks.

No.	m	n	b_1	b_2	b_3	b_4	b_5	b_6	$\|\mathbf{s}_1\|$	$\|\mathbf{s}_2\|$	$\|\mathbf{s}_3\|$	$\|\mathbf{s}_4\|$	$\|\mathbf{s}_5\|$	$\|\mathbf{s}_6\|$	$\angle\mathbf{s}_{12}$	$\angle\mathbf{s}_{13}$	$\angle\mathbf{s}_{45}$	$\angle\mathbf{s}_{56}$	$\angle\mathbf{s}_{14}$	$\angle\mathbf{s}_{15}$
E5	128	6	925.2	924.1	1046.8	1101.1	952.5	1016.9	290.9	295.8	291.3	297.2	282.5	297.9	91.75	90.57	91.05	89.25	45.05	51.54
		3	924.5	925.0	1047.0	1100.7	953.7	1016.8	290.7	295.7	291.4	297.0	281.9	298.0	91.86	90.42	91.22	89.30	–	–
	$\boldsymbol{\omega}=0$		926.9	923.6	1046.0	1100.0	953.4	1015.7												
E6	180	6	923.3	924.8	1041.8	1091.6	949.1	1014.8	290.2	294.8	290.8	293.5	285.9	297.3	90.22	89.80	90.89	89.32	46.15	50.81
		3	922.9	924.2	1041.1	1092.0	949.3	1014.5	289.7	294.4	290.7	294.2	285.1	297.0	90.31	89.88	90.81	89.16	–	–
	$\boldsymbol{\omega}=0$		927.4	925.1	1042.0	1094.7	952.3	1013.8												
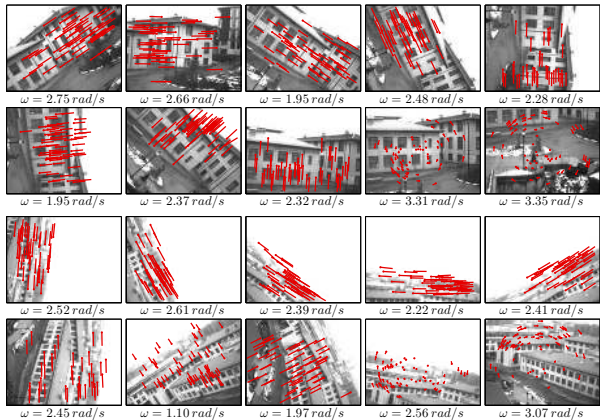
Fig. 18. Feature correspondences of distant scene points between two neighboring frames around the peaks in Fig. 19. The distance to the buildings is far greater than the amount of camera translation ($\rho \geq 500$). The buildings in E6 (bottom) are farther than those in the E5 (top) experiment.

Fig. 19. The output of six gyroscopes generated when the IMU is oscillated multiple times in different axes by a tripod. The output at each peak (indicated by arrows) is collected into the measurement matrix $\mathbf{Z}$.
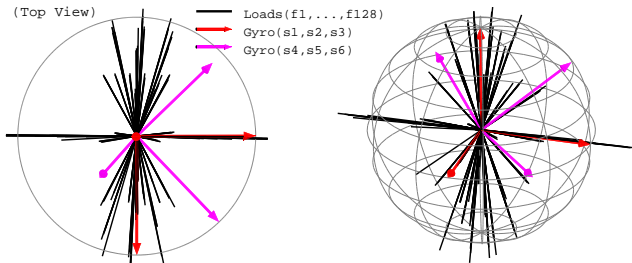
Fig. 20. The gyroscope's shape and motion matrix ($\mathbf{F}$ and $\mathbf{S}$) reconstructed from factorization-based redundant calibration ($n = 6$) in the E5 experiment. Each angular velocity in $\mathbf{F}$ has a different magnitud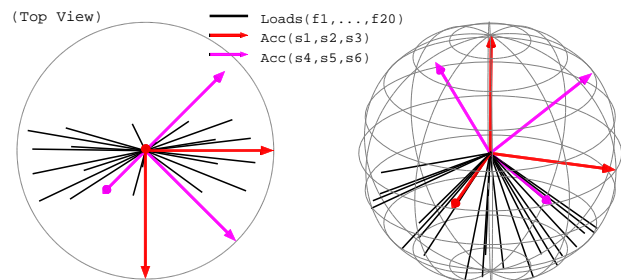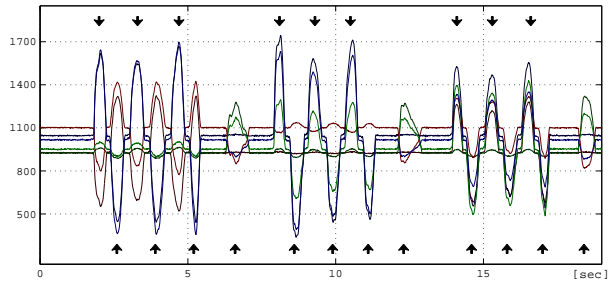e. Two tri-axial IMUs are ($\mathbf{s}_1, \mathbf{s}_2, \mathbf{s}_3$) and ($\mathbf{s}_4, \mathbf{s}_5, \mathbf{s}_6$).

TABLE VI. Comparison between factorization and two nonlinear methods for accelerometer calibration experiments (E1 to E4). The parameter difference Δ between factorization and nonlinear minimization is very small.

	Factorization		Constrained (E_{con})		Weighted (E_{wls})	
	E_Z	$E_\mathcal{C}$	E_Z	$E_\mathcal{C}$	E_Z	$E_\mathcal{C}$
E1	0.093	0.00088	0.136	0.00000	0.090	0.00076
E2	0.123	0.00060	0.163	0.00000	0.098	0.00079
E3	0.122	0.00074	0.167	0.00000	0.102	0.00094
E4	0.116	0.00086	0.151	0.00000	0.110	0.00087
	Param. difference		$\Delta\mathbf{b}$	$\Delta\|\mathbf{s}\|$	$\angle\mathbf{s}$	$\Delta\mathbf{b}$	$\Delta\|\mathbf{s}\|$	$\Delta\angle\mathbf{s}$
E1			0.003	0.045	0.002	0.001	0.031	0.001
E2			0.010	0.023	0.003	0.000	0.030	0.002
E3			0.024	0.036	0.006	0.003	0.027	0.002
E4			0.017	0.049	0.009	0.001	0.031	0.003
T	0.03 ± 0.02 sec		22.1 ± 9.9 sec		2.3 ± 0.8 sec	

$E_Z = \sum_{i,j=1}^{m,n}(\mathbf{f}_i^\top \mathbf{s}_j + b_j - z_{ij})^2$ and $E_\mathcal{C} = \sum_{(i,j)\in\mathcal{C}}^{k}(\mathbf{f}_i^\top \mathbf{f}_j - c_{ij})^2$
$\Delta\mathbf{b}$ is a mean difference of $\mathbf{b}$ after minimization (so are $\Delta\|\mathbf{s}\|$ and $\Delta\angle\mathbf{s}_{ij}$).
T is a computation time in seconds when implemented in MATLAB.

constituted the load constraint $\mathcal{C}^* = (\|\boldsymbol{\omega}_1\|, \ldots, \|\boldsymbol{\omega}_m\|)$ for the gyroscope calibration ($m = 128$ for E5, $m = 180$ for E6).

Table V compares gyroscope parameters found by the redundant and triad calibration, respectively, in exactly the same way as done in Table IV. Additional comparison is made for $\mathbf{b}$ obtained at a stationary condition ($\boldsymbol{\omega} = 0$). The estimated parameters are almost identical regardless of the calibration method at less than 0.3% deviation within each dataset.

The parameter variances between E5 and E6 are relatively large compared to the accelerometer case. This is because $\|\boldsymbol{\omega}_i\|$ in $\mathcal{C}^*$ has a limited accuracy due to a number of systematic errors from image processing. The calibration accuracy is expected to logarithmically increase as more load constraints are combined. In the accelerometer case, a relatively small number of motions is sufficient since the gravity magnitude is an absolute knowledge about applied motions.

Fig. 20 shows the reconstructed shape and motion matrix, $\mathbf{S}$ and $\mathbf{F}$, of the gyroscope unit. The distribution of $\mathbf{F}$ reveals that we rotated the IMU around the same axis multiple times but with different magnitudes.

C. Factorization method and nonlinear minimization

The IMU calibration can be casted as a nonlinear minimization problem [13]–[15]. Many solutions to this nonlinear problem are computationally complex due to high dimensionality ($\mathbf{F}$, $\mathbf{S}$ and $\mathbf{b}$) and require physically reasonable initial parameters to start with, which is not always straightforward to obtain in practice. So the factorization can serve as a good initializer for nonlinear methods.

We compared two cost functions, constrained function E_{con} and weighted least-squares function E_{wls}, depending on whether $\mathcal{C}$ is treated as hard or soft constraints as follows:

$$E_{con} = \sum_{i,j=1}^{m,n} (\mathbf{f}_i^\top \mathbf{s}_j + b_j - z_{ij})^2 \quad \text{s.t. } \mathbf{f}_i^\top \mathbf{f}_j = c_{ij} \text{ in } \mathcal{C} \quad (43)$$

$$E_{wls} = \sum_{i,j=1}^{m,n} \frac{(\mathbf{f}_i^\top \mathbf{s}_j + b_j - z_{ij})^2}{\sigma_{z_{ij}}^2} + \sum_{(i,j)\in\mathcal{C}}^{k} \frac{(\mathbf{f}_i^\top \mathbf{f}_j - c_{ij})^2}{\sigma_{c_{ij}}^2} \quad (44)$$

where σ_z and σ_c are variances of IMU measurements and load constraints, respectively.

Table VI shows nonlinear refinement results that begin with the parameters obtained from the factorization. In the constrained optimization on E_{con}, E_Z increases slightly due to the hard constraint $E_\mathcal{C} = 0$ but the parameter difference remains small. The difference between the weighted least-squares E_{wls} and the factorization is much smaller since the factorization also uses the soft constraint $\mathbf{Lq} = \mathbf{c}$ in (14). Note that when $\mathcal{C}$ consists of inferred measurements like camera images in the gyroscope case, E_{wls} is more appropriate since its minimum provides the maximum likelihood parameter estimate under Gaussian noise. A similar cost to E_{wls} is also used in *bundle adjustment* [35] in computer vision, which finds jointly optimal structure and camera poses in visual reconstruction.

From the fact that the parameter difference is nearly negligible in Table VI, we can conclude that factorization results are very close to a global optimum. The factorization is not only numerically stable but also at least a hundred times more computationally efficient than the nonlinear methods. Therefore, in cases where a limited computational resource prohibits those nonlinear methods, it would be sufficient to use the factorization-based calibration result.

X. Conclusion and Future Work

We have presented a new factorization-based approach to IMU self-calibration. Our factorization method is not only a linear solution but also applicable to any sensor configurations that a three-dimensional IMU may have. Given no prior information about calibration parameters, we provided an automatic calibration that only requires magnitudes of applied loads. The load of a known magnitude is readily attainable from natural references without external calibration devices. We demonstrated that gravity and distant scene objects captured by a camera are sufficient inputs for in-field or in-situ IMU calibration.

Since a measurement model is affine due to the bias, we thoroughly investigated the property of the factorization's reconstruction space to find a linear solution. We proved that the rank of the linear solution space varies depending on the constraint type, revealing that the gravity magnitude is subject to a one-dimensional null space. This rank analysis is also useful to identify degenerate load configurations and a minimum number of constraints.

In the factorization method, the number of sensor components is equal to a maximum dimension of linearly recoverable parameters. For redundant IMUs, we presented a linear method

that finds all the four-dimensional calibration parameters simultaneously. For triad IMUs, an iterative linear method was presented where an initial bias is required but possible to be automatically set as the mean of measurements due to its wide convergence region.

Compared to nonlinear optimization, the merits of the proposed factorization-based calibration include all the advantages that a linear solution offers such as no initial guess, local minima or heavy computation. The calibration accuracy and precision in the simulation and experiments is almost equivalent to those achieved by a nonlinear optimization.

One area for future work is an identification of scale factor nonlinearity. For gyroscopes, this would be achievable by repeating the factorization with different load magnitudes $\mathcal{C}_\tau^*$ while τ increments from 0 to a maximum range using a speed-controlled turntable.

Appendix A
Conversion Matrix $\mathbf{T}_{16\times10}$ and $\mathbf{T}_{9\times6}$

In the redundant IMU calibration, when the symmetric $\mathbf{Q}$ in (13) is parameterized by $\mathbf{q}$ as follows, $\mathbf{T}_{16\times10}$ is

$$\mathbf{q} = \begin{bmatrix} q_1 \\ q_2 \\ \vdots \\ q_{10} \end{bmatrix}, \quad \mathbf{Q} = \begin{bmatrix} q_1 & q_2 & q_3 & q_4 \\ q_2 & q_5 & q_6 & q_7 \\ q_3 & q_6 & q_8 & q_9 \\ q_4 & q_7 & q_9 & q_{10} \end{bmatrix} \quad (45)$$

$$\mathbf{T}_{16\times10} = \begin{bmatrix} 1 & & & & & & & & & \\ & 1 & & 1 & & & & & & \\ & & 1 & & & 1 & & & & \\ & & & 1 & & & & 1 & & \\ & & & & 1 & & & & & \\ & & & & & 1 & & 1 & & \\ & & & & & & 1 & & & 1 \\ & & & & & & & 1 & & \\ & & & & & & & & 1 & 1 \\ & & & & & & & & & 1 \end{bmatrix}^\top \quad (46)$$

In the triad IMU calibration, when the symmetric $\mathbf{Q}_{3\times3}$ in (38) is parameterized by $\mathbf{q}'$ as follows, $\mathbf{T}_{9\times6}$ is

$$\mathbf{q}' = \begin{bmatrix} q_1 \\ \vdots \\ q_6 \end{bmatrix}, \quad \mathbf{Q}_{3\times3} = \begin{bmatrix} q_1 & q_2 & q_3 \\ q_2 & q_4 & q_5 \\ q_3 & q_5 & q_6 \end{bmatrix} \quad (47)$$

$$\mathbf{T}_{9\times6} = \begin{bmatrix} 1 & & & & & \\ & 1 & 1 & & & \\ & & 1 & & 1 & \\ & & & 1 & & \\ & & & & 1 & 1 \\ & & & & & 1 \end{bmatrix}^\top \quad (48)$$

Appendix B
Orthogonal load constraint ($c_{ij} = 0$)

In addition to $\mathcal{C}^*$ in Section IV-A, the load constraint (6) also includes an inter-relation case c_{ij} ($i \neq j$), which would be hard to find from natural references. One simple and cheap way to obtain c_{ij} in practice is to use a right-angle iron shown in Fig. 21. This apparatus can rapidly produce a high volume of orthogonal load constraints ($c_{ij} = 0$) for both accelerometer
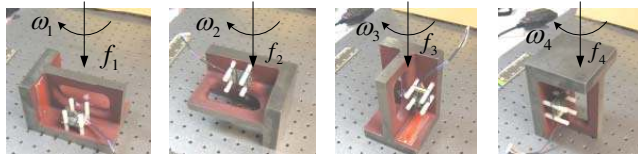
Fig. 21. A right-angle iron on a flat surface conveniently provides a set of orthogonal load constraints $c_{ij} = 0$ ($\mathbf{f}_1^\top \mathbf{f}_2 = \mathbf{f}_1^\top \mathbf{f}_3 = \cdots = 0$ or $\boldsymbol{\omega}_1^\top \boldsymbol{\omega}_2 = \boldsymbol{\omega}_1^\top \boldsymbol{\omega}_3 = \cdots = 0$).

and gyroscope calibration. Since all the adjacent surfaces of the right-angle iron are orthogonal, putting the iron on its six surfaces by turns ($\mathbf{f}_i^\top \mathbf{f}_j = 0$) or rotating the iron manually on a surface contact ($\boldsymbol{\omega}_i^\top \boldsymbol{\omega}_j = 0$) produces mutually orthogonal motions. See [18] for further details.

Appendix C
IMU coordinates in an external frame

In Section V-A, non-coordinate-specific load constraints (6) makes the coordinate rotation $\mathbf{R}$ chosen freely. When IMU coordinates $\mathcal{I}$ need to be specified with respect to an external frame $\mathcal{O}$, one simple case is that some of $(\mathbf{f}_1, \ldots, \mathbf{f}_m)$ are known in terms of $\mathcal{O}$ to determine $\mathbf{R}$. In general, the transformation ($\mathbf{R}$ and possibly a translation $\mathbf{T}$) between $\mathcal{I}$ and $\mathcal{O}$ can be obtained by hand-eye calibration [36]. Once an IMU is intrinsically calibrated by the factorization method, its relative motions are available from IMU mechanization in $\mathcal{I}$ when it moves. If corresponding motions are also obtained in $\mathcal{O}$, it is well known that the transformation between these two frames can be estimated by solving a problem in the form of $\mathbf{AX} = \mathbf{XB}$ [36].

References

[1] S. Sukkarieh, P. Gibbens, B. Grocholsky, K. Willis, and H. F. Durrant-Whyte, "A low-cost, redundant inertial measurement unit for unmanned air vehicles," *International Journal of Robotics Research*, vol. 19, no. 11, pp. 1089–1103, 2000.

[2] M. E. Pittelkau, "RIMU misalignment vector decomposition," in *AAS/AIAA Astrodynamics Specialist Conference and Exhibit*, Aug. 2004.

[3] S. Y. Cho and C. G. Park, "A calibration technique for a redundant IMU containing low-grade inertial sensors," *ETRI Journal*, vol. 27, no. 4, pp. 418–426, 2005.

[4] K. Parsa, T. Lasky, and B. Ravani, "Design and implementation of a mechatronic, all-accelerometer inertial measurement unit," *IEEE/ASME Transactions on Mechatronics*, vol. 12, no. 6, pp. 640–650, 2007.

[5] C.-W. Ho and P.-C. Lin, "Design and implementation of a 12-axis accelerometer suite," in *Proc. IEEE/RSJ Int'l Conf. on Intelligent Robots and Systems*, Oct. 2009.

[6] R. M. Rogers, *Applied Mathematics in Integrated Navigation Systems (AIAA Education Series)*, 2nd ed. AIAA, 2003.

[7] J. J. Hall and R. L. W. II, "Inertial measurement unit calibration platform," *Journal of Robotic Systems*, vol. 17, no. 11, pp. 623–632, 2000.

[8] J. W. Diesel, "Calibration of a ring laser gyro inertial navigation system," in *13th Biennial Guidance Test Symposium*, Oct. 1987.

[9] E. Nebot and H. Durrant-Whyte, "Initial calibration and alignment of low-cost inertial navigation," *Journal of Robotic Systems*, vol. 16, no. 2, pp. 81–92, 1999.

[10] A. Kim and M. F. Golnaraghi, "Initial calibration of an inertial measurement unit using an optical position tracking system," in *IEEE Position Location and Navigation Symposium (PLANS 2004)*, Apr. 2004.

[11] Z. Dong, G. Zhang, Y. Luo, C. C. Tsang, G. Shi, S. Y. Kwok, W. Li, P. Leong, and M. Y. Wong, "A calibration method for mems inertial sensors based on optical tracking," in *2nd IEEE Int'l Conf. on Nano/Micro Engineered and Molecular Systems*, 2007.

[12] A. Lai, D. A. James, J. P. Hayes, and E. C. Harvey, "Semi-automatic calibration technique using six inertial frames of reference," in *Proceedings of the SPIE*, vol. 5274, 2004, pp. 531–542.

[13] I. Skog and P. Handel, "Calibration of a MEMS inertial measurement unit," in *XVII IMEKO World Congress*, Brazil, Sep. 2006.

[14] Z. F. Syed, P. Aggarwal, C. Goodall, X. Niu, and N. El-Sheimy, "A new multi-position calibration method for MEMS inertial navigation systems," *Measurement Science and Technology*, vol. 18, no. 7, pp. 1897–1907, 2007.

[15] S. P. Won and F. Golnaraghi, "A triaxial accelerometer calibration method using a mathematical model," *IEEE Transaction on Instrumentation and Measurement*, vol. 59, no. 8, pp. 2144–2153, 2010.

[16] R. M. Voyles, J. D. Morrow, and P. K. Khosla, "Shape from motion approach to rapid and precise force/torque sensor calibration," in *Int'l Mechanical Eng Congress and Exposition*, Nov. 1995, pp. 2171–2175.

[17] ——, "Including sensor bias in shape from motion calibration and sensor fusion," in *IEEE Multisensor Fusion and Integration Conference*, Dec. 1996.

[18] M. Hwangbo and T. Kanade, "Factorization-based calibration method for mems inertial measurement unit," in *Proc. IEEE Int'l Conf. on Robotics and Automation*, San Hose, USA, Apr. 2008.

[19] C. Tomasi and T. Kanade, "Shape and motion from image streams under orthography: a factorization method," *International Journal of Computer Vision*, vol. 9, no. 2, pp. 137–154, 1992.

[20] R. I. Hartley and A. Zisserman, *Multiple View Geometry in Computer Vision*, 2nd ed. Cambridge University Press, 2004.

[21] M. H. V. Grewal and R. Miyasako, "Application of kalman filtering to the calibration and alignment of inertial navigation systems," in *Proc. of the 29th IEEE Conf. on Decision and Control*, Dec. 1990, pp. 5–7.

[22] P. Zhang, J. Gu, E. E. Milios, and P. Huynh, "Navigation with IMU/GPS/Digital compass with unscented kalman filter," in *Proc. of the IEEE Conf. on Mechatronics and Automation*, 2005, pp. 1497–1502.

[23] F. M. Mirzaei and S. I. Roumeliotis, "A Kalman filter-based algorithm for IMU-camera calibration: Observability analysis and performance evaluation," *IEEE Trans. on Robotics*, vol. 24, no. 5, pp. 1143–1156, 2008.

[24] J. Hol, T. Schon, and F. Gustafsson, "Relative pose calibration of a spherical camera and an IMU," in *7th IEEE/ACM Int'l Symposium on Mixed and Augmented Reality (ISMAR 2008)*, Oct. 2008, pp. 21–24.

[25] J. Kelly and G. S. Sukhatme, "Visual-inertial sensor fusion: Localization, mapping and sensor-to-sensor self-calibration," *International Journal of Robotics Research*, vol. 30, no. 1, pp. 56–79, Jan 2011.

[26] T. Kanade and D. Morris, "Factorization methods for structure from motion," *Philosophical Transactions: Mathematical, Physical and Engineering Sciences*, vol. 356, pp. 1153–1173, 1998.

[27] K. Kim, Y. Sun, R. M. Voyles, and B. J. Nelson, "Calibration of multi-axis mems force sensors using the shape-from-motion method," *IEEE Sensors Journal*, vol. 7, no. 3, pp. 344–350, 2007.

[28] Y. Sato, M. D. Wheeler, and K. Ikeuchi, "Object shape and reflectance modeling from observation," in *Annual Conference on Computer Graphics*, 1997, pp. 379–387.

[29] G. H. Golub and C. F. V. Loan, *Matrix Computations*, 3rd ed. The Johns Hopkins University Press, 1996.

[30] Analog Device, *ADXL203 Precision Dual-Axis iMEMS Accelerometer*, Mar. 2006. [Online]. Available: http://www.analog.com/en/sensors/inertial-sensors/adxl203/products/product.html

[31] C. Harris and M. Stephens, "A combined corner and edge detector," in *Proceedings of the 4th Alvey Vision Conference*, 1988, pp. 147–151.

[32] J. Shi and C. Tomasi, "Good features to track," in *IEEE Conf. on Computer Vision and Pattern Recognition*, Seattle, Jun. 1994.

[33] B. D. Lucas and T. Kanade, "An iterative image registration technique with an application to stereo vision," in *Proceedings of the 7th International Joint Conference on Artificial Intelligence*, Vancouver, Canada, 1981, pp. 674–679.

[34] M. Hwangbo, J.-S. Kim, and T. Kanade, "Inertial-aided KLT feature tracking for a moving camera," in *Proc. IEEE/RSJ Int'l Conf. on Intelligent Robots and Systems*, 2009, pp. 1909–1916.

[35] B. Triggs, P. McLauchlan, R. Hartley, and A. Fitzgibbon, "Bundle adjustment – a modern synthesis," in *Vision Algorithms: Theory and Practice*, ser. Lecture Notes in Computer Science. Springer Berlin, 2000, vol. 1883, pp. 153–177.

[36] K. Daniilidis, "Hand-eye calibration using dual quaternions," *International Journal of Robotics Research*, vol. 18, pp. 286–298, 1998.

Myung Hwangbo is currently a postdoctoral fellow at Robotics Institute at Carnegie Mellon University. He received his B.S. and M.S. degrees in Mechanical Engineering from Pohang University of Science and Technology (POSTECH) in 1995 and 1997, respectively, and Ph.D. degree in Robotics from the Robotics Institute at Carnegie Mellon University in 2012. His Ph.D. thesis work was to automate a small-fixed wing unmanned aerial vehicle for autonomous navigation in an urban environment using low-cost sensors. He works in IMU-camera calibration, sensor fusion, geometry-based computer vision, sampling-based motion planning, and navigation algorithms for autonomous robots. His current research interests include a wearable first-person-vision device.

Jun-Sik Kim is currently a Senior Research Scientist at Korea Institute of Science and Technology (KIST). He received his B.S. degree in Electronic Engineering from Yonsei University in 1999, and M.S. and Ph.D. degrees in Electrical Engineering and Computer Science from KAIST in 2001 and 2006, respectively. After about one year as a post-doctor for KAIST, he worked for the Robotics Institute at Carnegie Mellon University as a Postdoctoral Fellow and a Project Scientist for five and half years. He works in computer vision, computer graphics, and intelligent robots. Specific research topics include sensor calibration, three-dimensional reconstruction, sensor fusion, camera motion tracking, image sensor noise modeling, and acceleration using parallelized hardwares.

Takeo Kanade is the U. A. and Helen Whitaker University Professor of Computer Science and Robotics at Carnegie Mellon University and currently directs the Quality of Life Technology Center. He received his Doctoral degree in Electrical Engineering from Kyoto University, Japan, in 1974. He was the Director of the Robotics Institute from 1992 to 2001. He also founded the Digital Human Research Center in Tokyo and served as the founding director from 2001 to 2010. Dr. Kanade works in multiple areas of robotics: computer vision, multi-media, manipulators, autonomous mobile robots, medical robotics and sensors. He has written more than 400 technical papers and reports in these areas, and holds more than 20 patents.

Dr. Kanade has been elected to the National Academy of Engineering and the American Academy of Arts and Sciences. He is a Fellow of several professional organizations, including the IEEE, the ACM, and the American Association of Artificial Intelligence (AAAI). Awards he received include the Franklin Institute Bower Prize, ACM/AAAI Allen Newell Award, Okawa Award, NEC Computer and Communication Award, Tateishi Grand Prize, Joseph Engelberger Award, IEEE Robotics and Automation Society Pioneer Award, and Azriel Rosenfeld Lifetime Accomplishment Award of International Conference of Computer Vision.